INVESTIGATION ON THE MECHANICAL PROPERTIES OF SMA-FIBER REINFORCED CONCRETE

A dissertation submitted in partial fulfillment of the requirements for the award of the

degree of

MASTERS OF ENGINEERING

IN

STRUCTURAL ENGINEERING

Submitted by:

DEEPAK RAJ

(802124009)

Under the Supervision of

Dr. Trishna Choudhury

(Assistant Professor)

CIVIL ENGINEERING DEPARTMENT
THAPAR INSTITUTE OF ENGINEERING & TECHNOLOGY
(DEEMED TO BE UNIVERSITY), PATIALA, PUNJAB

JULY, 2023

DECLARATION

I, Deepak Raj, hereby affirm that the research work presented in this thesis titled " **INVESTIGATION ON THE MECHANICAL PROPERTIES OF SMA-FIBER REINFORCED CONCRETE**" which is submitted to fulfill the requirements for the degree of Master of Engineering in Structural Engineering at the Civil Engineering Department of Thapar Institute of Engineering & Technology (Deemed to be University), Patiala, is a genuine and original piece of work conducted under the guidance of **Dr. Trishna Choudhury**, Assistant Professor in the Department of Civil Engineering, Thapar Institute of Engineering & Technology, Patiala, from January 2023 to July 2023. I confirm that the contents of this thesis have not been submitted, in part or in full, to any other university or institute for the purpose of obtaining any other degree.

Dated: 29 July 2023

Deepak Raj

Deepak Raj

(802124009)

CERTIFICATE

This is to certify that the above declaration made by the student concerned is correct to the best of my knowledge and belief.

Dr. Trishna Choudhury

Assistant Professor

Civil Engineering Department

TIET, Patiala, Punjab

ACKNOWLEDGMENT

With a profound commitment to excellence in learning and management, I am delighted to present this report, and I extend my heartfelt appreciation to all individuals and organizations who directly or indirectly contributed to its completion through their support, encouragement, and valuable advice.

First and foremost, I express my deep gratitude to my supervisor, Dr. Trishna Choudhury, Assistant Professor in the Civil Engineering Department at Thapar Institute of Engineering and Technology, Patiala. Her unwavering involvement, invaluable guidance, and continuous motivation were pivotal in the successful completion of this work, and I am truly indebted to her. This report demanded dedication, hard work, and sincerity, and I did my utmost to invest these qualities in the project, leading to significant personal growth and knowledge. I would like to express my sincere gratitude to Dr. Dhirendra Pandey, Assistant Professor, NIT Agartala and Mr. Akshay Sharma, a Ph.D. Scholar in the Civil Engineering Department, for his valuable guidance and support throughout this endeavor. Additionally, I am humbly grateful to my friends, Rahul Kumar, Ayush Kumar, Anshul Sharma, and Nitish Kumar for their cheerful support during the casting and testing of specimens in the laboratory.

Moreover, I would like to acknowledge the invaluable contribution of Guru Nanak Dev Engineering College (GNDEC), Ludhiana, in the testing phase of this project. The support provided by GNDEC Ludhiana's technical staff and resources significantly enhanced the quality and reliability of the experimental results. Their commitment to academic collaboration played a vital role in the successful execution of this research.

Above all, I want to thank my parents for their boundless love and blessings, which have been a constant source of inspiration in transforming this manuscript into a reality. The people mentioned above, including the support from GNDEC Ludhiana, hold a special place in my heart and will always be remembered with fondness. Thank you all for being an integral part of this journey.

Deepak Raj

(802124009)

ABSTRACT

The use of innovative materials and structural configurations is of significant interest in modern engineering applications. This study presents a comparative analysis of the pull-out performance between Shape Memory Alloy (SMA) and steel reinforcement wires with two different end configurations: hooked and straight end shape. The aim is to evaluate the influence of end shape on the bond behavior and pull-out strength of these materials.

Experimental investigations were conducted using pull-out (bond) tests on SMA fibers embedded in high strength concrete specimens under room temperature and for specimens heated to elevated temperatures. The tests were performed under controlled laboratory conditions, ensuring consistent testing parameters for accurate comparisons. Pull-out force and slip behavior were recorded and analyzed for each configuration. The results indicated that the end shape configuration significantly influenced the bond behavior and pull-out strength of both SMA and steel reinforcement wires. The hooked end configuration demonstrated superior performance, exhibiting higher peak pull-out forces and more ductile behavior compared to the straight configurations. The selection of the appropriate end-shape configuration can significantly influence the bond behavior and pull-out strength, thereby impacting the structural performance and serviceability of reinforced concrete elements.

The results of this study contribute to the understanding of SMA fibers' behavior under pull-out loading conditions and inform engineers and researchers in making informed decisions regarding material selection and end configuration design. Further research is recommended to investigate the long-term behavior, durability, and compatibility of these materials with different structural systems and environments.

TABLE OF CONTENT

LIST OF TABLES

Table No. **Description** **Page No.**

LIST OF FIGURES

Fig No. **Description** **Page No.**

LIST OF ABBREVIATIONS

SMA : Shape Memory Alloy.

BI : Base Isolation.

RB : Rubber Bearing.

TMD : Tuned Mass Dampers.

NiTi : Nickel-Titanium.

UHPC : Ultra High Performance Concrete.

HSC : High Strength Concrete.

f_{ck} : Compressive Strength of Concrete.

f_y : Yield Strength of Steel.

A_s : Austenite start temperature.

A_f : Austenite finish temperature.

M_s : Martensite start temperature.

M_f : Martensite finish temperature.

E_A : Modulus of elasticity in the Austenite phase.

E_M : Modulus of elasticity in the Martensite phase.

τ_{max} : Maximum Shear stress

τ_{eq} : Equivalent bond strength

d_f : Diameter of fibre

L_{em} : Embedded length

W_p : pullout energy

W/b : Water – binder ratio

CHAPTER 1

INTRODUCTION

1.1 OVERVIEW

The study aims to contribute to the understanding of the mechanical characteristics of Shape Memory Alloys (SMA) and facilitate the adoption of SMA as a reinforcing material. The scope of the study includes conducting laboratory experiments to evaluate the bond strength between concrete and SMA fibres, and analysing the mechanical properties of materials.

1.2 THE SHAPE MEMORY ALLOYS (SMA)

SMA is a metallic alloy that exhibits the unique property of shape memory effect, wherein it can return to its original shape after being deformed when subjected to a specific stimulus, typically temperature change. This behavior is attributed to a reversible phase transformation that occurs within the alloy's microstructure. The most used SMA is Nitinol (Song et al., 2006), which is composed of Nickel (Ni) and Titanium (Ti) in roughly equal proportions. Nitinol has a martensitic phase at lower temperatures and an austenitic phase at higher temperatures. When heated above a certain temperature called the austenite finish temperature (A_f), Nitinol transits from its deformed martensitic phase to its original austenitic phase and recovers its original shape as shown in **Figure 1.1**.

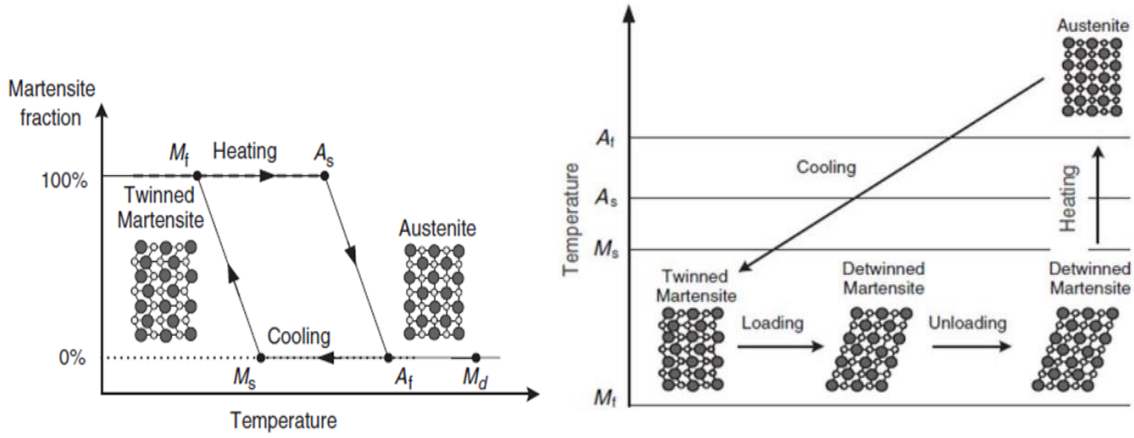

(a) (b)

Figure 1.1. SMA transition showing both stress and temperature effect – ((a) Ozbulut et al., 2011; (b) Ozbulut et al., 2011)

Figure 1.1 (a) depicts that Shape Memory Alloys (SMAs) undergo phase transformations between austenite and martensite at specific temperatures. As the SMA is heated, it starts

changing from twinned martensite to austenite at the Austenite Start Temperature (A_s) and fully reverts to its original shape at the Austenite Finish Temperature (A_f). Upon cooling, the reverse transformation from austenite to twinned martensite begins at the Martensite Start Temperature (M_s), and it is completed at the Martensite Finish Temperature (M_f). The critical temperature, Martensite Start Temperature (M_d), represents the threshold above which the martensite phase cannot be induced by an applied load.

Figure 1.1 (b) depicts that when the alloy is deformed in the martensitic phase, twinned martensite transforms into detwinned martensite. If the alloy is unloaded at a temperature below the Martensite Finish Temperature (M_f), it will remain in the detwinned phase. However, when the alloy is heated above the Austenite Finish Temperature (A_f), it undergoes a transformation back to the austenitic phase and recovers its original shape. On cooling, the alloy transforms back to the twinned martensite phase and it is known as shape memory effect.

SMA alloys offer unique properties that make them versatile and valuable in a wide range of industries and applications. Ongoing research and development continue to explore new uses and enhance the performance of SMA materials.

1.3 MAJOR CONCERNS AND MOTIVATION OF THE STUDY

To address the challenges faced in strengthening and repairing reinforced concrete (RC) structures, researchers have developed various materials and techniques. These include corrosion-resistant steel plates, high-performance cementitious composites, externally bonded fiber-reinforced polymer (FRP) jackets, and near-surface-mounted (NSM) FRP sheets. Another promising option gaining attention is the Shape Memory Alloys (SMA) due to their unique properties, namely superelasticity (SE) and the shape memory effect (SME). Several studies (Czaderski et al., 2019; Zareie et al., 2020) have highlighted the application of SMA for the strengthening and repair of RC structures.

Over the past two decades, researchers worldwide have shown increased interest in seismic control. Recent earthquakes have highlighted the collapse of buildings due to inadequate mitigation of seismic forces. When a structure's fundamental frequency aligns with the dominant frequency range of earthquake ground motions, vibrations are amplified, causing stress on structural members beyond their design limits. This can result in permanent damage or even the collapse of the entire structure. Non-structural components may also be affected, leading to injuries and financial losses.

Base isolation (BI) is a cost-effective method that decouples the superstructure from ground motions, preventing amplification. Elastomeric, frictional, and roller bearings are commonly used in base isolation, but they have limitations. Semi-active techniques, such as viscous fluid and magneto-rheological dampers, have been tested to address these issues. Several researchers (Gu et al., 2019; Chen et al., 2014; Fu et al., 2019; Rabiee et al., 2019; and Li et al., 2019) have developed control algorithms for magneto-rheological dampers that show satisfactory suppression of seismic waves.

SMA, on the other hand has found applications in engineering, medicine, and other industries (Dezfuli et al., 2014; Jani et al., 2014). Shape memory alloys (SMA) possess attractive properties, including shape memory effect, superelasticity, and high strain recovery rate, making them suitable for seismic control applications as shown in **Figure 1.2**. The shape memory effect of SMA alloys makes them useful in various applications, including biomedical devices, Actuators, Robotics Aerospace and Defense, as well as customer products. SMA alloys are widely used in medical applications, such as stents, dental braces, and orthopedic implants. SMA wires and springs are used as actuators in robotic systems and industrial automation for precise and controllable motion. SMA materials find applications in aerospace engineering, such as in aircraft components, deployable structures, and adaptive control systems, owing to their lightweight, high strength, and shape-changing capabilities. Nonetheless, several consumer products, such as eyeglass frames and other novelty items have found its application due to its ability to bend and return to their original shape.

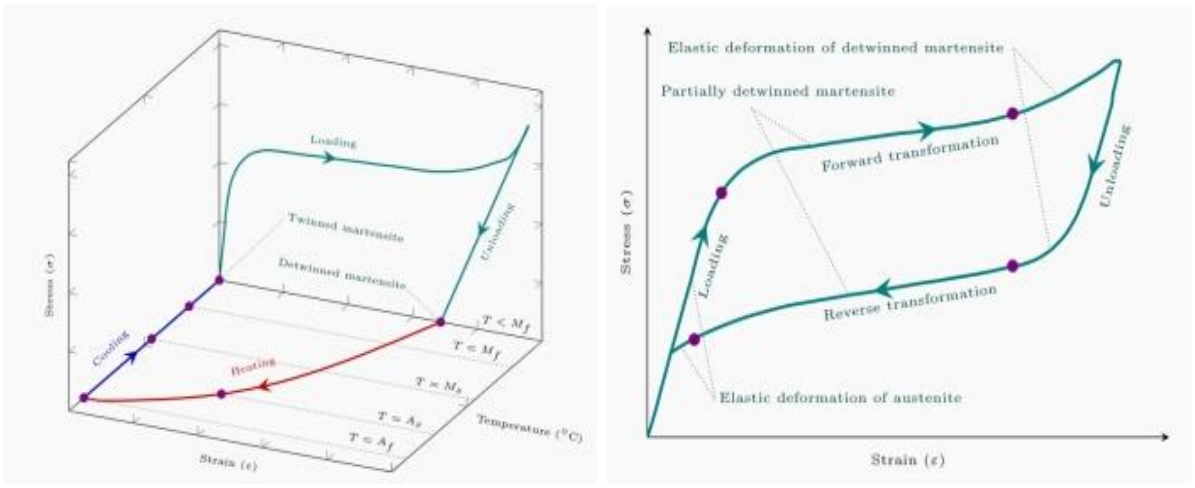

(a) (b)

Figure 1.2 Stress–strain–temperature curves for: (a) SME; (b) PE ((a) Tabrizikahou et al., 2022; (b) Tabrizikahou et al., 2022)

In the field of Civil Engineering also, SMA can be a boon because of its unique characteristics, such as the ability to retain its original shape even after experiencing significant strains of up to 13.5% when subjected to heating or stress (Dezfuli et al., 2014). SMA wire-reinforced concrete structures are being explored to improve the seismic performance of buildings and bridges. The shape memory effect of SMA allows them to provide self-centering and energy dissipation that make them well-suited for control applications during seismic events.

Several studies have highlighted the effectiveness of shape memory alloys (SMAs) in various applications for seismic protection and structural resilience in bridge engineering. Choi et al. (2006) proposed an innovative bridge isolation system using SMA wires and elastomeric bearings, which demonstrated improved seismic performance surpassing conventional lead-rubber bearings. Saiidi and Wang (2006) emphasized the importance of SMA bars as longitudinal reinforcement in concrete columns, showcasing their ability to recover deformations post-yielding and the effectiveness of engineering cementitious composites (ECC) in repairing SMA-reinforced columns. Saiidi et al. (2009) highlighted the superiority of SMA bars in reinforcing concrete bridge columns, exhibiting enhanced cyclic response, increased ductility, and improved energy dissipation capacity. Andrawes et al. (2010) demonstrated the importance of SMAs in seismic retrofitting of RC bridge columns, showing superior performance compared to carbon fiber-reinforced polymer (CFRP) retrofitting. Dezfuli et al. (2014) found that incorporating SMA wires in elastomeric isolators significantly enhanced lateral stiffness and reduced residual deformation in Composite fiber-reinforced high-damping rubber bearings (CFR-HDRBs), although limitations were observed in re-centering capability. Collectively, these studies highlight the promising potential of SMAs in enhancing seismic protection and structural performance in bridge engineering.

1.4 OBJECTIVES OF THE PRESENT STUDY

Based on the literature study conducted on the use of SMA in civil engineering field, following preliminary objectives are considered.

- **Quantify Bond Strength:** Measure and quantify the bond strength between high-strength concrete and SMA using pull-out tests.
- **Understand Bond Behavior under thermal effects:** Investigate the bond strength behavior governing the high-strength concrete and SMA under the effect of elevated temperature.

By addressing these objectives within the defined scope, the research findings can contribute to advancing the understanding of bond behavior between high-strength concrete and SMA and facilitate the adoption of SMA reinforcement in structural engineering.

1.5 ORGANISATION AND OUTLINE OF THESIS

To carry out the considered objectives, the present thesis is divided into **five chapters** and is structured as follows:

Chapter 1 serves as the Introduction, providing an overview of SMA (Shape Memory Alloy) and addressing the key concerns and motivations behind the study. It includes a brief summary about SMA, outlines the objectives of the research, and sets the stage for the subsequent chapters.

Chapter 2 presents a comprehensive review of previous research conducted on reinforcing SMA and steel fibers in concrete. The primary focus is on examining the bond behavior between high-strength concrete and SMA. Through this review, the need for the current research is identified based on the existing gaps and limitations in the literature.

Chapter 3 delves into the materials used for the experimental samples, the design composition of the specimens, and the methodology employed to carry out the experiments. It provides a detailed explanation of the materials' selection process, the composition of the samples, and the experimental procedures followed in order to obtain reliable data.

Chapter 4 discusses the results obtained from the experimental investigations conducted on fiber-reinforced concrete. It analyzes the outcomes of the tests performed and presents various conclusions drawn from the experimental findings. This chapter provides an in-depth discussion of the results, their implications, and their alignment with the research objectives. **Chapter 5** gives an overall summary and concludes the present study.

CHAPTER 2

LITERATURE REVIEW

2.1 GENERAL

This chapter presents a comprehensive literature review on the utilization of shape memory alloy (SMA) fibers in high-strength concrete, with a specific emphasis on examining the bond strength. The review explores the various parameters and shapes of steel and SMA fibers and their impact on bond strength. Additionally, it highlights the significant applications of SMA fibers in the construction field. By comparing the performance of steel and SMA fibers and considering different influencing factors, this literature review provides valuable insights into the potential of SMA fibers and their role in enhancing the strength and durability of concrete structures.

2.1.1 Historical background of SMA

Shape Memory Alloys (SMAs) have a fascinating historical background that spans several decades. The discovery of the shape memory effect dates to 1932 when Swedish scientist Arne Olander observed the unique behavior of a gold-cadmium alloy. However, it was not until the 1960s that the term "shape memory" was coined by the researchers at the Naval Ordnance Laboratory (NOL) in the United States.

In the early 1960s, researchers at NOL, including William Buehler and Frederick Wang, extensively studied the shape memory effect in various metal alloys. They focused on the nickel-titanium (NiTi) alloy, which exhibited remarkable shape memory properties. NiTi alloy, also known as Nitinol, was initially developed for use in the aerospace industry, but its unique shape memory and superelastic characteristics soon found applications in various fields.

Throughout the 1970s and 1980s, extensive research was conducted to understand the underlying mechanisms of SMAs and explore their potential applications. This period saw significant advancements in SMA materials, including the development of new alloys and improved processing techniques. The discovery of the pseudoelasticity phenomenon in SMAs, where they exhibit large elastic deformations without permanent deformation, further expanded their application possibilities.

In the following decades, SMAs found numerous applications in various industries, including aerospace, automotive, biomedical, robotics, and civil engineering. Their ability to undergo

reversible deformations, recover their original shape, and exhibit high strength and durability has made them valuable for actuators, sensors, dampers, and other innovative devices.

2.2 SMART MATERIALS IN A CONSTRUCTION INDUSTRY

Shape Memory Alloys (SMAs) have diverse applications in the construction industry. They are used as seismic dampers, adaptive facades, self-adjusting joints, smart windows, and active roofing systems. SMAs provide enhanced structural resilience, energy efficiency, and versatility in architectural design. They can also be embedded in concrete for self-healing capabilities and utilized in shape-changing structures. With their high strength, lightweight nature, and ability to return to their original shape, SMAs contribute to improved structural performance and functionality in construction.

2.2.1 Seismic retrofitting

SMAs can be employed to retrofit buildings and bridges to improve their resistance to earthquakes. SMA-based dampers can be installed in critical structural elements to absorb and dissipate seismic energy, reducing the risk of structural damage and enhancing overall seismic performance.

Yang et al. (2010) introduced an innovative hybrid device that merges re-centering Shape Memory Alloy (SMA) wires with energy-absorbing steel struts. This device also incorporates two robust steel tubes to facilitate the controlled movement of the SMA wires and struts. The combination of these components allows for enhanced structural performance, enabling the device to efficiently re-center after deformation and effectively absorb and dissipate energy, making it a promising solution for structural engineering applications.

Speicher et al. (2009) introduced a specialized seismic retrofitting device illustrated in **Figure 2.1**. This device was designed to enhance the structural performance of buildings during earthquakes. It incorporated either NiTi helical springs or NiTi Belleville washers in its compression mechanism. Through repeated loading tests, they observed that the helical springs displayed desirable properties of returning to their original position after deformation, known as re-centering, while also providing effective damping. This re-centering capability made them suitable for restoring the device's initial state. In contrast, the Belleville washers exhibited efficient energy dissipation characteristics, making them a valuable choice for absorbing and dissipating energy within a Shape Memory Alloy (SMA)-based system.

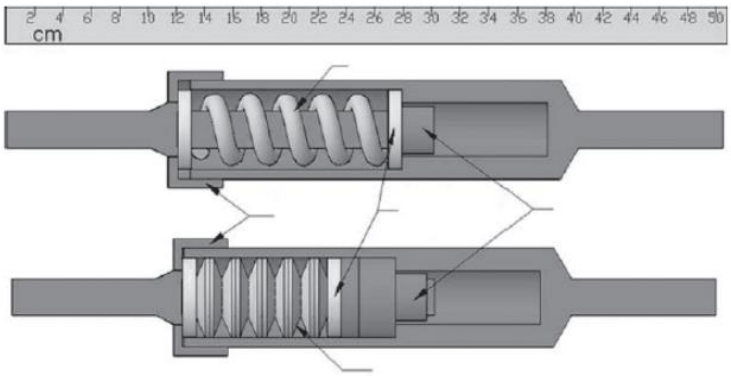

Figure 2.1 SMA tension/compression device (Speicher et al., 2009).

Ma and Cho et al. (2008) presented a damper design utilizing shape memory alloy (SMA) wires that are pre-tensioned for energy dissipation and two pre-compressed springs for restoring force. Numerical studies were performed to verify the anticipated performance of the device. The findings indicated that a 1 m long damper can achieve an equivalent damping ratio of 12% with a displacement stroke of 30 mm, while maintaining full re-centering capability. This research underscores the potential of SMA-based dampers in effectively dissipating energy, providing valuable insights for the development of innovative damping solutions in structural engineering applications.

Van de Lindt and Potts (2008) introduced an SMA-based device, designed to mitigate the seismic response of wood frame structures. The device comprises an inner tube and an outer tube, with two studs connected to the inner tube and one stud connected to the outer tube. SMA wires are installed between these studs and pre-strained. This configuration allows the device to provide enhanced damping and energy dissipation during seismic events, contributing to improved structural performance and resilience which is shown in **Figure 2.2**. This research highlights the potential of SMA-based devices for enhancing the seismic resistance of wood frame structures.

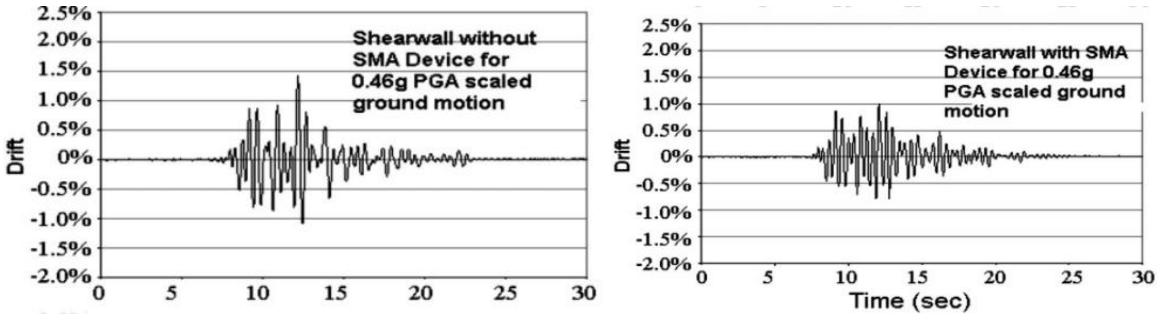

Figure 2.2 Time history responses interstory drift for the 0.46g Canoga Park record (Van de Lindt and Potts, 2008).

Li et al. (2008) developed two SMA-based devices in which SMA wires were consistently subjected to elongation. The performance of these devices was investigated through shake table tests conducted on a five-story steel frame structure. The objective of the study was to assess the effectiveness of the SMA-based devices in enhancing the seismic response of the structure. The research findings provided valuable insights into the behavior and performance of the devices under dynamic loading conditions, demonstrating their potential for improving the seismic resilience of steel frame structures.

Han et al. (2005) introduced a shape memory alloy (SMA) damper capable of operating in tension, compression, and torsion. The damper utilized superelastic NiTi wires that experienced tensile strains under all loading conditions. To validate the effectiveness of the damper for various types of motion, analytical and experimental investigations were conducted using three scaled-down damper models. This research demonstrates the versatility and potential of the SMA damper in effectively dampening tensile, compressive, and torsional motions, providing valuable insights for the development of innovative damping solutions in engineering applications.

2.2.2 Structural reinforcement

SMAs can be embedded or attached to existing structural elements to reinforce their strength and stiffness. By applying an external stimulus, such as heat or an electrical current, the SMAs can change their shape and provide additional support to vulnerable sections of the structure, improving overall load-carrying capacity.

Beam - Column Joint (BCJ)

DesRoches et al. (2010) conducted a study on the seismic performance of steel frames with beam-to-column connections incorporating Shape Memory Alloy (SMA) bars. They investigated two types of connections: a superelastic SMA connection with re-centering capability and a martensitic SMA connection with energy dissipation capacity. Numerical models of these connections were developed and validated using experimental test results. Non-linear time history analyses were performed on three- and nine-story moment-resisting frames. It was found that standard PR (Post and Beam) connections exhibited greater predicted peak and residual deformation demands when compared to buildings equipped with SMA (Shape Memory Alloy) connections. The results showed that SMA connections were highly effective in controlling the structural response, particularly under high seismic intensity and it can be seen in **Figure 2.3**. In a related study, the researchers carried out a probabilistic seismic

demand analysis to statistically evaluate the efficacy of SMA connections in steel moment-resisting frames **(Ellingwood et al., 2010).**

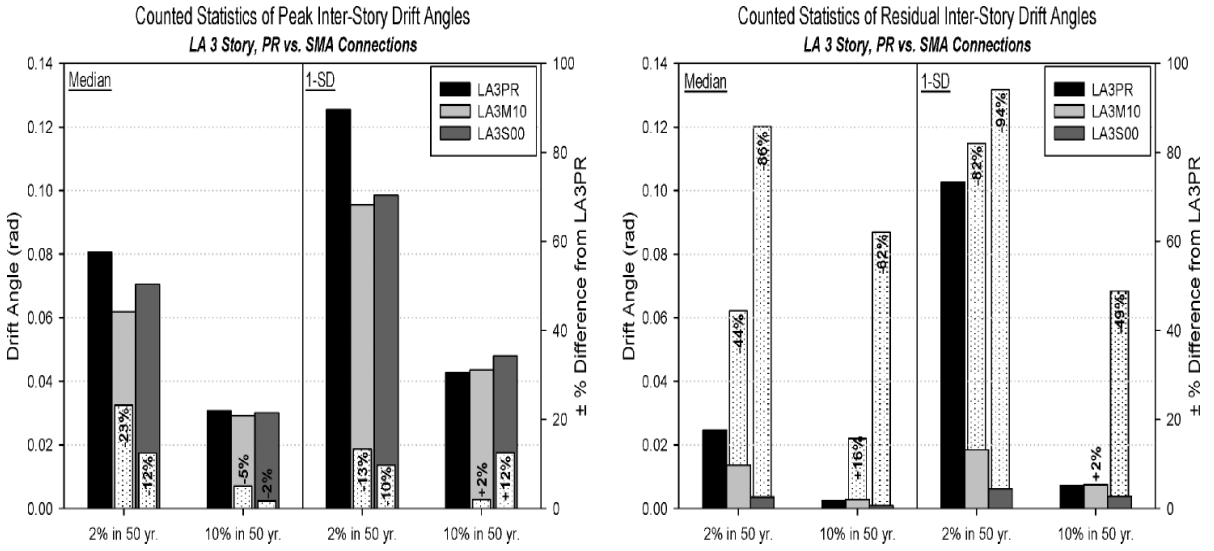

Figure 2.3 Statistics of (a) peak (left) and (b) residual (right) inter-story drift demands for LA 3-story model structure with PR and SMA connections. Percentage increases from the uncontrolled PR case are shown as white bars. (DesRoches et al., 2010)

Sepulveda et al. (2008) conducted an experimental study on a partially restrained steel beam-column connection utilizing CuAlBe Shape Memory Alloys (SMAs). The researchers subjected a prototype of the connection to cyclic testing at frequencies of 0.25 and 1 Hz. The results showed that the connection exhibited stable cycles with equivalent damping ratios of up to 5.5%. Importantly, the SMA bars in the connection experienced negligible residual strains after deformation, indicating the effectiveness of the CuAlBe SMAs in maintaining their structural integrity and performance.

Youssef et al. (2008) conducted a study investigating the use of superelastic Shape Memory Alloys (SMAs) as reinforcement in beam-column joints of reinforced concrete (RC) structures. Two large-scale beam-column joint specimens were tested, one reinforced with conventional steel rebars and the other reinforced with NiTi longitudinal rebars combined with steel rebars. The results indicated that SMA-reinforced joints exhibited lower energy dissipation capacity and bond strength to concrete compared to steel joints. However, the SMA-reinforced joints showed significant recovery of post-yield deformation, unlike steel joints that experienced substantial residual drifts. This suggests that SMA joints can remain functional even after strong earthquakes. In another study, the same researchers developed a numerical model capable of simulating the behavior of SMA-reinforced RC beam-column joints **(Alam et al., 2008)**.

Ma et al. (2007) investigated a self-centering beam-to-column connection utilizing superelastic Shape Memory Alloys (SMAs). The connection design included an extended end-plate, long shank SMA bolts, continuity plates, beam-flange ribs, and web stiffeners. Through finite element modeling and numerical simulations using ANSYS, the researchers predicted the behavior of the connection. Results showed that the SMA connection exhibited excellent energy dissipation characteristics and the ability to recover 94% of its total deformation. Importantly, the connection also avoided local buckling in the connecting beam, a common issue observed in traditional connections throughout the loading process.

Ocel et al. (2004) studied the performance of partially restrained steel beam-column connections was experimentally evaluated using martensitic Shape Memory Alloys (SMAs). Four large diameter NiTi bars were utilized as primary moment transfer mechanisms, connecting the beam flange to the column flange. Quasi-static and dynamic cyclic loading tests were performed on two full-scale SMA-based connections. By heating the SMA bars above the transformation temperature, the shape memory effect was initiated after the initial test. The results showed that the SMA connections were able to recover approximately 76% of the beam tip displacement, demonstrating their capability to effectively mitigate deformation in the connections.

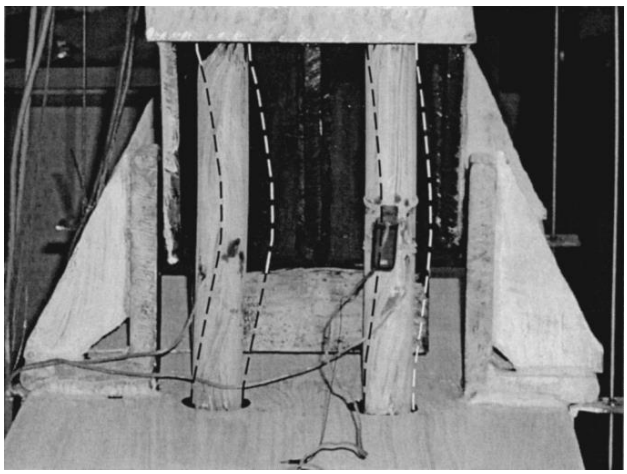

Figure 2.4 Photo of connection S2 tendons after heating; dashed lines represent residual shape before heating (Ocel et al., 2004**)**

2.2.3 Shape memory braces

In retrofitting applications, SMAs can be utilized as shape memory braces. These braces can be installed to provide additional lateral stability and resistance against wind or seismic forces. The SMA braces can actively adjust their shape and stiffness to optimize the structural response and mitigate potential damage.

Huang et al. (2018) proposed a seismic mitigation approach using NiTi Shape Memory Alloy (SMA) helical springs and steel wire as an energy dissipation brace system for frame structures. They tested a two-story steel frame retrofitted with four SMA springs through numerical simulations and vibration table experiments. The results demonstrated superior attenuation of displacement and acceleration responses compared to steel spring and viscous damper systems. However, under the Kobe Earthquake scenario, the performance of SMA bracing was similar to steel bracing for certain ground accelerations, highlighting the uncertainty in SMA bracing's behavior under different seismic conditions. This study highlights the potential of SMA-based bracing for seismic mitigation while emphasizing the need for further investigation into their performance under diverse earthquake scenarios.

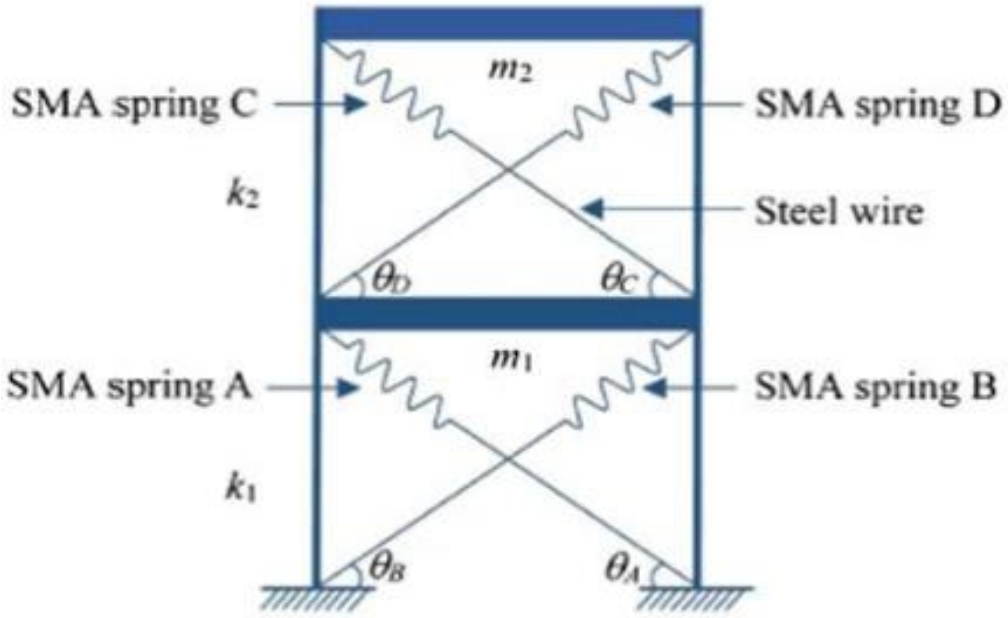

Figure 2.5 Mechanical model of frame structure with 4 SMA springs (Huang et al., 2018)

Cortés-Puentes et al. (2018) retrofitted squat reinforced shear walls using tension-only NiTi Shape Memory Alloy (SMA) bracing. Four 1/3rd scale wall models (two with controlled bracing, two with SMA bracing) were subjected to reverse cyclic testing. The retrofit significantly improved seismic performance by enhancing strength, energy dissipation, and drift capacity. SMA braces exhibited a negative elongation of approximately 33 mm during out-of-plane damage, while SMA links had less than 5 mm elongation, highlighting their limited capability in accommodating such displacements. The research advances the understanding of using SMA bracing systems for retrofitting shear walls and provides insights for enhancing the seismic resilience of existing structures.

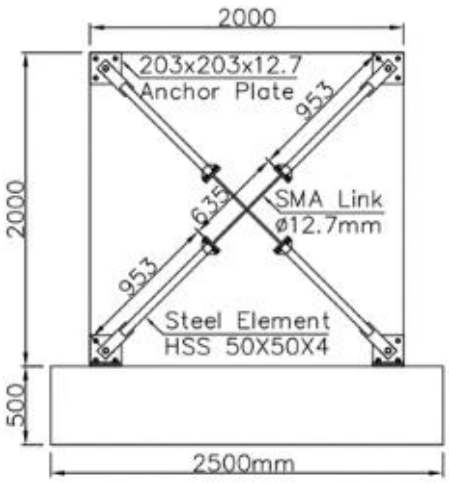

Figure 2.6 Walls retrofitted with SMA bracings (Cortés-Puentes et al., 2018)

Gao et al. (2016) developed a braced damping device comprising a Shape Memory Alloy (SMA) ring and four cables. To prevent abrasion fracture, a hard rubber layer was introduced between the steel cable and SMA ring. Experimental testing on a full-scale bracing system was conducted to calibrate the Abaqus finite element model. The loading resulted in a significant reduction in the diameter along the centroid, with a deformation of approximately 79.3% from 230 mm to 47.6 mm. Despite the large deformation, the SMA ring exhibited high ductility and re-centering capacity with minimal residual deformations. However, the tension-only behavior of the SMA ring limited the compressive action from the steel cables towards the center. Numerical models were developed and validated to simulate mechanical properties and loading curves, providing a basis for future development of SMA elements.

Zhou et al. (2016) conducted a study on self-centering buckling restrained braces, investigating the hysteretic performance of linear-elastic and Shape Memory Alloy (SMA) pretension rods. They developed a cyclic elastoplastic flow chart based on rheological analysis and focused on parameters such as post-tensioning element material, pre-tension, pretension rod area, core plate cross-section area, and initial brace stiffness, studying their effects on hysteretic performance.

Zhu et al. (2008) presented a friction damping brace element utilizing superelastic Nitinol wires. The Nitinol wires acted as a recentering component, while energy dissipation occurred through friction. Nonlinear time-history analysis and pushover analysis were conducted on two model buildings, demonstrating a significant reduction in residual story drifts and improved seismic performance through friction damping. However, the models considered in this study were not specifically optimized for self-centering friction damping braces, but rather for buckling restrained braces.

2.2.4 Vibration control

SMAs can also be employed in retrofitting projects for vibration control. By incorporating SMA-based devices, such as tuned mass dampers or vibration absorbers, into structures, unwanted vibrations can be reduced or eliminated, improving occupant comfort and protecting the integrity of the building.

SMA Based TMD (Tuned Mass Dampers)

Several numerical testing results demonstrated that SMA coil springs can effectively reduce vibration on the TMD. Practical SMA-TMDs, on the other hand, are uncommon in the literature.

Huang et al. (2020) investigated the use of Cu-Al-Mn Shape Memory Alloy (SMA) as a connecting rod in a Tuned Mass Damper (TMD) system. The experiment involved a two-story scaled-down steel structure of 1.2 meters in height, subjected to dynamic testing on a shaking table. The advantage of using SMA in the TMD design was the ease of retuning the damper by increasing the temperature of the SMA when reducing the structural mass. However, the effectiveness of this approach was limited by the diminishing damping effect as the temperature of the SMA rose. This finding highlights the importance of considering the temperature-damping relationship in SMA-based TMD systems to optimize their performance.

Huang et al. (2018) conducted an investigation to enhance the understanding of pseudoelastic behavior in Shape Memory Alloy (SMA) springs. The researchers explored multiple tests that influence pseudoelasticity, such as spring processing technology, geometric dimension, and loading mode, aiming to contribute to comprehensive research in this field. The study extensively analyzed the force-displacement curves of SMA springs under complex dynamic loads. The findings provide valuable insights into the behavior of SMA springs and contribute to advancing the knowledge and application of SMA technology in various fields.

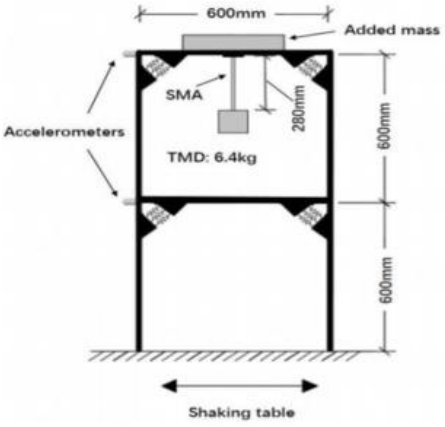

Figure 2.7 Frame structure with SMA-TMD (Huang et al., 2020)

Mishra et al. (2013) suggested the utilization of a nonlinear Shape Memory Alloy (SMA) spring within a conventional Tuned Mass Damper (TMD) system as an efficient approach to mitigate seismic vibrations. The researchers conducted extensive numerical simulations, employing stochastic linearization of SMA hysteresis and nonlinear random vibration analysis. Through the optimization of the structure's root mean square displacement, they obtained optimal design parameters for the SMA spring. This study provides valuable insights into the application of SMA technology in TMD systems for effective seismic vibration control and contributes to the advancement of structural engineering practices.

2.3 PROPERTIES OF SMA

Two key properties of SMAs are Shape Memory Effect (SME) i.e. removal of stress. The exhibition of these peculiar properties is a result of the two main phases present in SMA. These phases have different crystal structures, namely martensite, and austenite. Austenite is the parent phase stable at higher temperatures and lower stresses. Martensite is the secondary product phase stable at lower temperatures and higher stresses. So, based on the application of stress or variation temperature, the shifting between these crystalline phases takes place giving rise to the key properties mentioned above. Further, Martensite can be present in two different forms based on the crystal arrangement, namely twinned form and detwinned form. The graphical representation of these different phases can be seen in **Figure 2.8**. The reorientation of martensite variants i.e. detwinning is also gaining interest in the study of SMA behaviour lately.

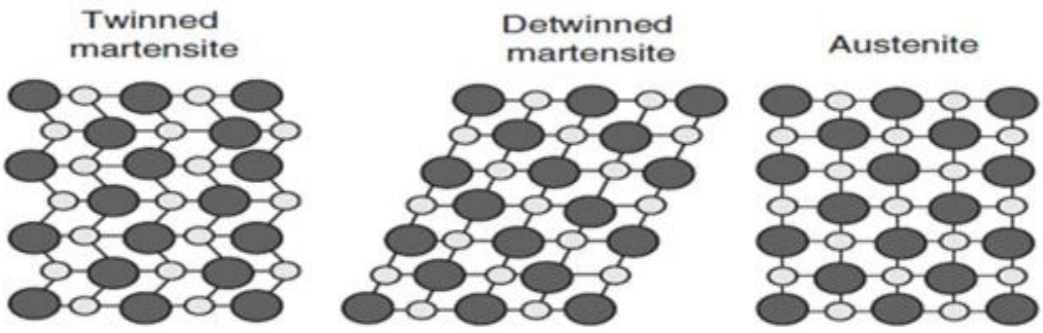

Figure 2.8 Different Phases of SMA (Ozbulut et al., 2011)

Martensite fraction is displayed as a function of temperature (in absence of external stress) in **Figure 2.9**. Four characteristic temperatures are represented, namely A_s (Austenite start temperature), A_f (Austenite finish temperature), M_s (Martensite start temperature), and M_f (Martensite finish temperature). Upon heating, a material starts its transformation from twinned martensite to austenite at A_s and completes its transformation at A_f. Then, upon cooling, the

reverse transformation from austenite to twinned martensite begins at M_s and the transformation 3 is finished at M_f. M_d is the critical temperature above which the transformation to the martensite phase cannot be induced by an applied load.

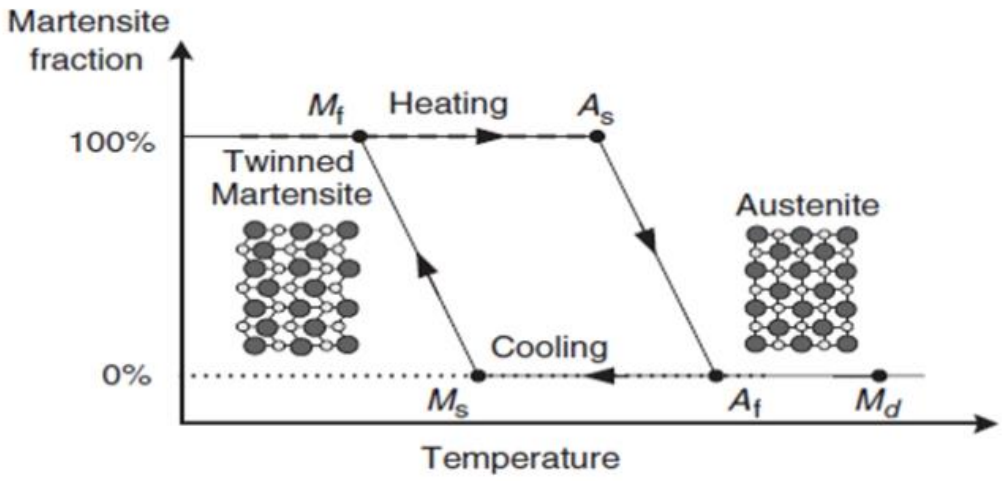

Figure 2.9 Martensite fraction-temperature diagram of SMAs (Ozbulut et al., 2011)

2.3.1 Mechanical Properties of SMA

Shape Memory Effect (SME) - The ability of the alloy to return from deformed shape to its initial shape upon heating is known as Shape Memory Effect. When the deformation is taken place in the martensitic phase, twinned martensite transforms to detwinned martensite. If it is unloaded at a temperature below the M_f, then it will remain in the same detwinned phase. Now, if the alloy is heated to a temperature more than A_f, the material can be seen recovering to the austenitic phase. If the alloy is cooled, then it transforms back to the twinned martensite phase. The illustration of this Shape Memory Effect is shown in **Figure 2.10**.

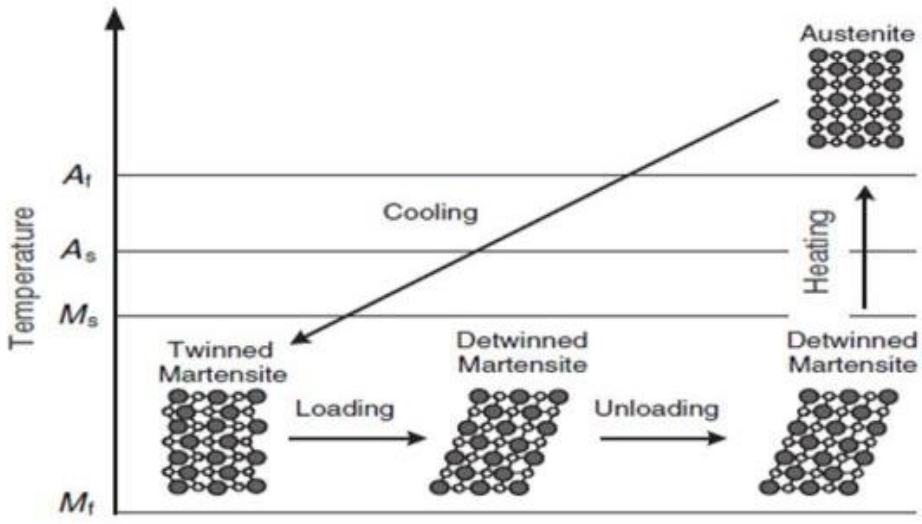

Figure 2.10 Shape memory effect (Ozbulut et al., 2011)

Super Elastic Effect (SE) - The ability of a material to recover large amounts of strain under constant temperature is known as the Super Elastic Effect. At temperatures as high as A_f, the SMA will be in its austenite phase. The direct transformation from austenite to detwinned martensite takes place when sufficiently large stress is applied at this temperature. When the stress is removed, complete shape recovery takes place by reverse transformation to the austenite phase. The illustration of this Super Elastic Effect is shown in **Figure 2.11.**

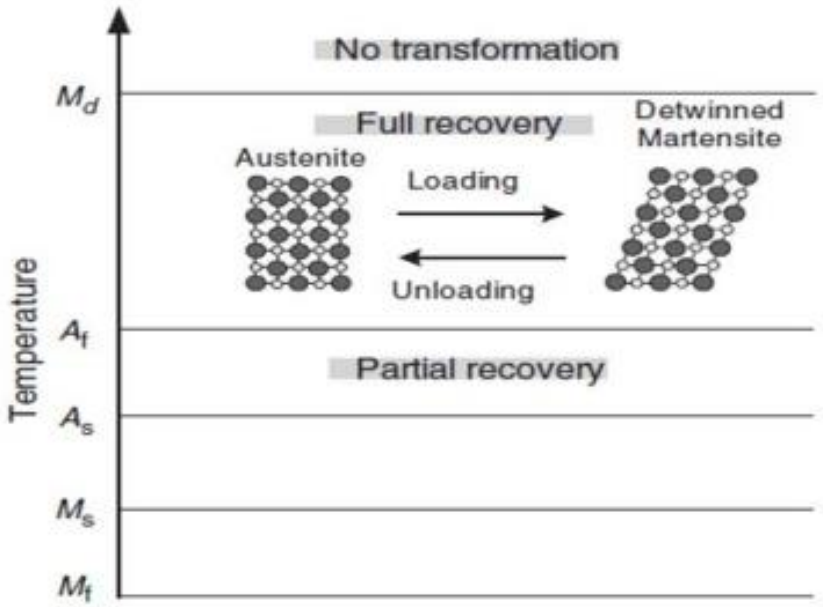

Figure 2.11 Super elastic effect (Ozbulut et al., 2011)

2.3.2 Physical Properties of SMA

Table 2.1 Properties of SMA (Zareie et al., 2020)

Physical Properties	**Value**
Melting Point (°C)	1310
Density (g/cm^3)	6.5
Electrical resistivity (ohm-cm)	82
Modulus of Elasticity (GPa)	41-75
Coefficient of thermal expansion (/°C)	11x10^-6
Ultimate Tensile Strength	1070
Total Elongation	10%

2.3.3 Mechanics of SMA

When the temperature is equal to or greater than the austenitic finish temperature ($T \geq A_f$), SMA material exhibit the superelasticity effect. **Figure 2.12** shows the stress-strain curve for loading and unloading of an SMA material.

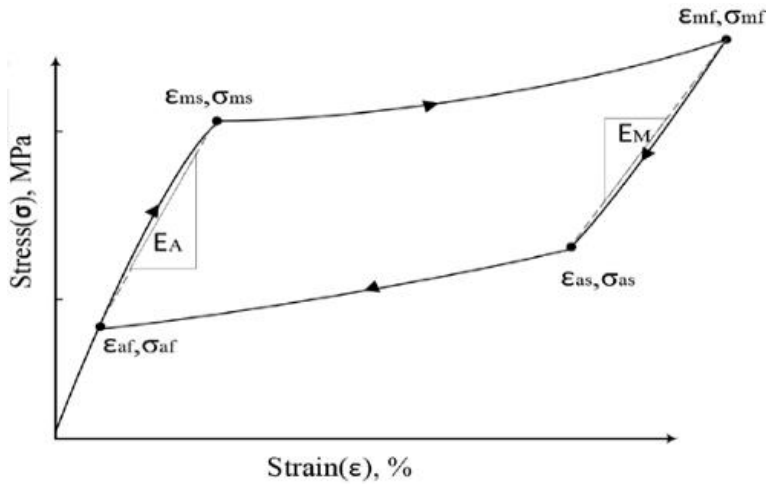

Figure 2.12 Hysteresis of SMA (Zareie et al., 2020)

In the loading phase, there are two parts: linear and plastic, whereas in the unloading process, material exhibits three portions, huge stress reduction with negligible strain reduction, huge strain reduction, huge strain reduction with a small amount of stress, and finally linear stress strain reduction. It is noted that the area under the stress strain curve describes the energy dissipation property of the SMA when loading and unloading. E_A indicates the modulus of elasticity in austenite phase; similarly, for linear unloading stage where the material is in full martensite phase, modulus of elasticity is defined by E_M. For other regions, modulus of elasticity is a combination of E_A and E_M as in Eq (1). Further unloading beyond this point produces a linear elastic behavior to zero stress- strain.

$$E = E_A + (E_M - E_A)\xi \tag{1}$$

2.3.4 Different types of SMA

Although the shape memory effect has been discovered in NiTi a long time ago (in 1963) and a significant amount of research has been carried out in finding similar alloys, only NiTi-based alloys, Cu-based alloys, and Fe-based alloys have found the commercial applications. The NiTi-based alloys are the most studied SMA and they are used in the forms of wires, rods, plates, and springs. Sometimes, NiTi is also referred to as Nitinol, derived from its alloy composition (NiTi) and place of origin (Naval Ordinance Laboratory). In Nitinol, Nickel and Titanium are present in the ratio of 51:49 respectively. As the composition of Nickel raises

above 50%, the transformation temperature decreases subsequently. Thus, the transformation temperature can be adjusted by modifying the alloy composition. Cu-based alloys are comparably low-priced than NiTi-based alloys as it is easy to machine them.

However, the strain recovery rate is low at 2-4%. There are various alloy combinations with Cu that exhibit SMA properties. Commonly used base binary alloys are CuAl and CuZn with the third metal varying as per the particular property enhancement. CuZnAl exhibits high ductility, so as the recently identified CuAlMn-based SMA (Sutou et al., 2008). CuZnNi is less sensitive to the aging effect. Unlike NiTi, few Cu-based alloys exhibit a wide range of transformation temperature, for example, CiAlBe exhibits superelastic behavior from -65° to 180°C. Fe-based SMAs have a very high recoverable strain rate compared to any other SMA. Fe-based SMA also reduces the cost by a significant amount. FeNCATB can experience up to 13.5% strain. FeMnSi has a very high strength that helps in the dislocation motion and slightly lower degree of SME.

2.4 FIBRES IN CONCRETE

2.4.1 Steel fibres in concrete

Abdallah et al. (2016) focused on the pull-out behavior of hooked end steel fibers embedded in ultra-high-performance mortar. The impact of end hook geometry and fiber inclination angle on the pull-out response was thoroughly investigated. Results showed that the pull-out behavior of both straight and hooked end fibers was directly influenced by the end hook geometry and inclination angle. While the tensile strength of straight fibers did not significantly impact the pull-out behavior, the variation in end hook geometry and tensile strength of hooked end fibers led to significant differences. Increasing both the tensile and anchorage strength of 4D and 5D fibers had a major influence on the pull-out behavior, resulting in higher maximum pull-out load and work compared to 3D and 4D fibers. The optimal inclination angle for the highest pull-out load and work was 15°, although fiber rupture tended to occur at larger inclination angles. Overall, the hooked end fibers exhibited a high utilization of their tensile capacity, particularly the 4D fibers which can be easily seen in **Figure 2.13**.

Bouazaoui and Li et al. (2008) found that using an adhesive joint between the steel and concrete surfaces significantly improved the strength of the connection by distributing shear and tensile stresses more effectively. The ultimate force of the connection depended on the diameter and embedded length of the steel rod, as well as the bonded surface area. Cracking in the concrete started at the embedded end of the steel rod and spread both transversely and longitudinally. The average shear stress estimation was not accurate in depicting the actual

shear stress distribution. The proposed model in this study revealed that the critical shear stress at the onset of concrete cracking ranged from 4.5 to 6.1 MPa, and the maximum shear stress to applied tensile stress ratio was approximately 0.05 for a 12 mm steel rod diameter.

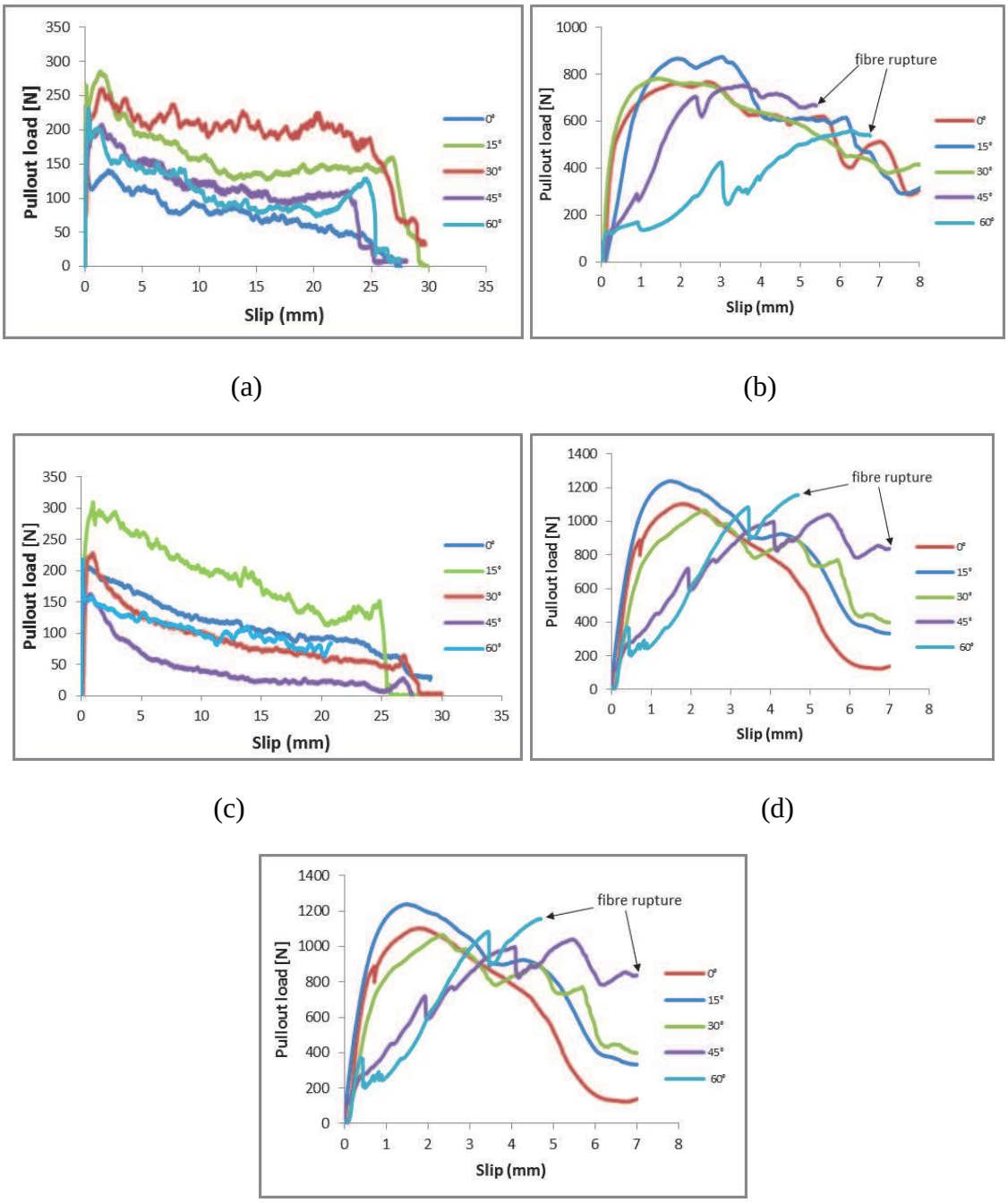

Figure 2.13 Average pullout-slip curves for:(a)3D; (b)5D straight end steel;(c) 3D; (d) 4D and (e) 5D hooked end steel fibers embedded in UHPFRM at different inclination angles. (Abdallah et al., 2016)

Bouazaoui and Li et al. (2008) found that using an adhesive joint between the steel and concrete surfaces significantly improved the strength of the connection by distributing shear

and tensile stresses more effectively. The ultimate force of the connection depended on the diameter and embedded length of the steel rod, as well as the bonded surface area. Cracking in the concrete started at the embedded end of the steel rod and spread both transversely and longitudinally. The average shear stress estimation was not accurate in depicting the actual shear stress distribution. The proposed model in this study revealed that the critical shear stress at the onset of concrete cracking ranged from 4.5 to 6.1 MPa, and the maximum shear stress to applied tensile stress ratio was approximately 0.05 for a 12 mm steel rod diameter.

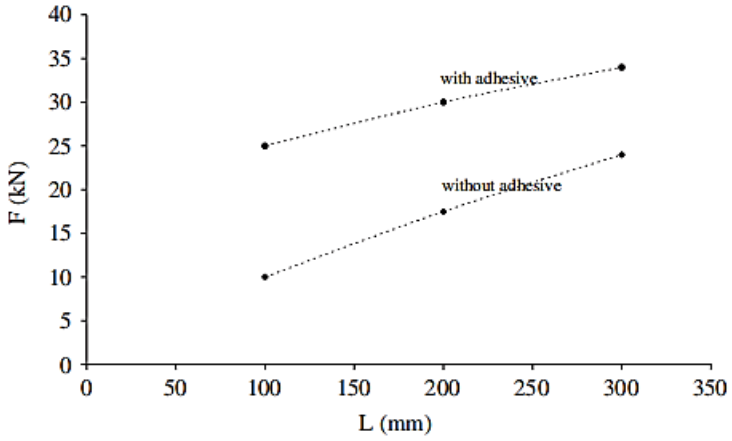

Figure 2.14 Comparison of ultimate load for the structures with and without adhesive joint between the steel rod and concrete surfaces (d = 12 mm) (Bouazaoui and Li et al., 2008)

2.4.2 SMA fibres in concrete

Qian et al. (2023) examined the shear behavior of RC short columns confined by superelastic SMA wires. The findings revealed that confining the columns with SMA wires shifted the failure mode from shear to bending, resulting in improved bearing capacity, ductility, and energy dissipation. The self-centering capacity was influenced by the initial pre-strain of the SMA wires. Higher pre-strain levels within the range of 0-2% enhanced performance, while pre-strain levels of 2-4% had an adverse effect. Increasing the SMA configuration rate improved shear capacity, ductility, energy dissipation, and self-centering capacity. Axial compression ratios consider 30-60 positively impacted various performance indicators, except for an axial compression ratio of 80, which had some detrimental effects. Overall, confining RC short columns with superelastic SMA wires can enhance seismic performance, but careful consideration of parameters is crucial for optimal results.

Hoult and Almeida et al. (2022) -This study investigated the seismic performance of planar RC walls reinforced with SMA rebars. SMA-reinforced walls exhibited strain concentration at the base, while steel-reinforced walls allowed for plasticity spread. Tensile strains were

observed in the lightly reinforced web of SMA walls due to the different Young's modulus. Crack distribution confirmed strain concentration near the base. The Bernoulli-Euler assumption reasonably simulated strain profiles, but nonlinear branches were observed for steel-reinforced walls. The SMA-reinforced walls showed a spike in tensile strains at the boundary ends. The equivalent plastic hinge length remained constant for SMA walls, but steel walls had a shorter hinge length due to premature base crack formation.

Wang et al. (2020) investigated the superelastic property of NiTi SMA fibers in self-compacting concrete (SCC), comparing them with steel and PP fibers. The results showed that NiTi SMA fiber-reinforced SCC had suitable fresh properties and displayed the largest deformed strain. While NiTi SMA fiber had moderate pull-out performance, steel fibers outperformed in terms of energy absorption and post-crack behavior. Higher volume fractions of NiTi SMA and steel fibers led to improved performance, whereas PP fibers showed lower strength and volume fraction. We can say that NiTi SMA fibers exhibited unique superelastic properties, but steel fibers demonstrated superior energy absorption and post-crack behavior in SCC.

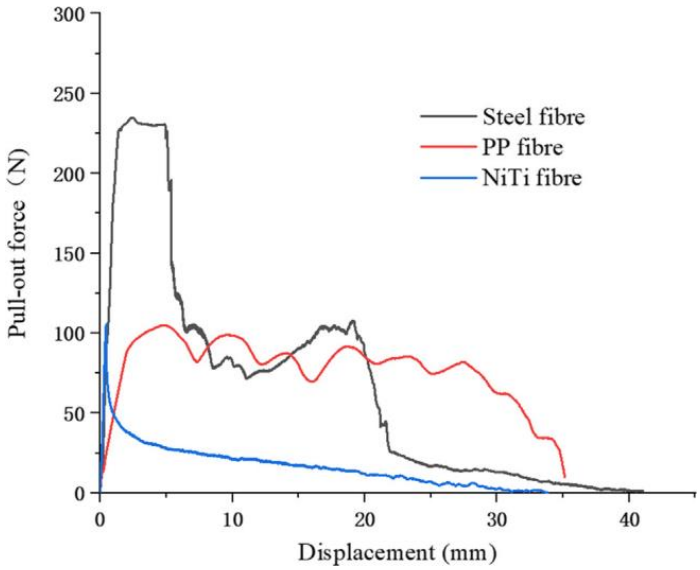

Figure 2.15 Pull-out strength of the NiTi SMA, steel and PP fibres. (Wang et al., 2020)

Feng et al. (2019) examined the impact of seven types of steel fibers on the pullout behavior of steel fibers embedded in an MPC-based matrix. Smaller diameter fibers with a brass coating surface demonstrated higher pullout resistance, efficient crack-bridging behavior, and improved bond strength and energy absorption. Fibers with deformation along their length exhibited higher mechanical bond contribution compared to hooked-end fibers. The failure mode depended on factors such as fiber surface roughness and deformations, resulting in

different failure modes. A decrease in fiber spacing led to a slight reduction in pullout load, fiber stress, bond strength, and energy absorption. The group effect of fibers weakened the bond as spacing decreased. These findings contribute to understanding the behavior and bond characteristics of steel fibers in an MPC-based matrix.

Sherif et al. (2018) investigated the flexural behavior of hybrid fiber reinforced concrete using SMA and steel fibers. Straight SMA fibers showed poor bond behavior and excessive pullout, limiting re-centering capabilities. However, SMA fibers exhibited better crack-width control than steel fibers. Hybrid fiber-reinforced specimens had lower residual displacement, improved crack closure, and slightly higher flexural strength. Combining SMA and steel fibers increased energy dissipation, and equal volume ratios improved fiber distribution. The study recommended using SMA fibers with end hooks for enhanced mechanical anchorage and flag-shape superelastic response, leading to improved re-centering and crack-closing properties.

Shahverdi et al. (2016) investigated the potential of strengthening reinforced concrete beams using ribbed Fe-SMA bars embedded in an additional shotcrete layer. Promising results were obtained, including the successful manufacture of ribbed Fe-SMA bars, activation through resistive heating, and strain measurements using digital image correlation. The beams demonstrated uplifts and recovery stresses indicating the feasibility of prestressing with iron-based SMAs. The beams with ribbed Fe-SMA bars exhibited higher cracking loads and increased loading capacity compared to those with steel ribbed bars. Ribbed Fe-SMA bars were easily prestressed without the need for mechanical jacks or ducts in the concrete. Further research is being conducted to address shotcrete shrinkage and investigate methods to reduce shrinkage cracks. More experiments are required to thoroughly explore this issue.

Choi et al. (2014) investigated the potential of using straight Shape Memory Alloy (SMA) fibers for reinforcing cement composites, highlighting several key findings. Prestrained SMA wires displayed the ability to recover both their diameter and elongated length. Cold-drawn SMA fibers demonstrated higher bond strength compared to reference SMA fibers due to their relatively larger Young's modulus. By heating the prestrained SMA fibers within mortar, the diameter expansion caused bulging, leading to increased normal confining pressure on the fiber and subsequently, higher bond strength. The dog-bone-shaped SMA fiber, heated only at the ends, exhibited a bond strength similar to that of the SMA fiber heated inside the mortar, making it more practical for field applications. This shape provided anchoring action at the bulged ends rather than relying solely on increased confining pressure. Further research is needed to assess the SMA fibers' capability to close and cure cracks in concrete beams.

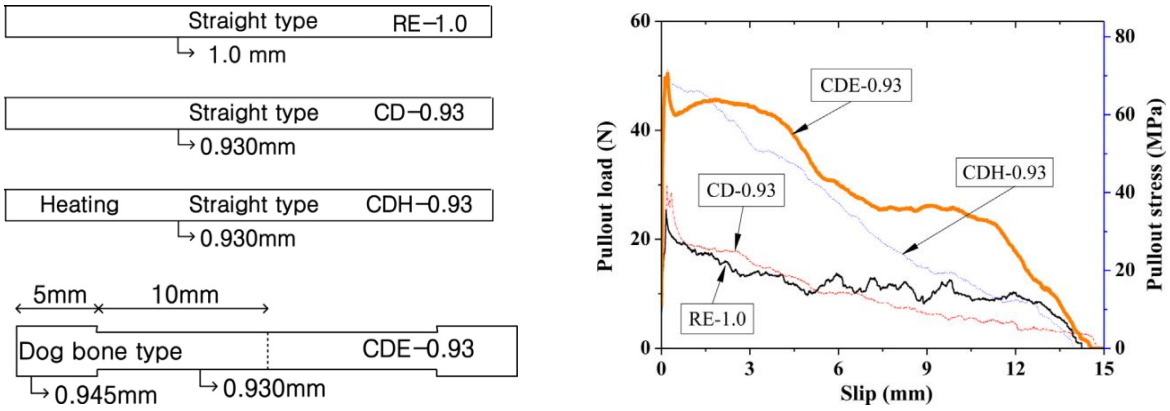

(a) (b)

Figure 2.16 (a) Dimension and shapes of Fiber; (b) Force–slip curves of specimens**.** (Choi et al., 2014)

Choi et al. (2010) investigated the bond strength of concrete confined by NiTiNb SMA wire jackets. It was observed that the bond stress to initiate radial cracks was the same for plain and confined concrete. However, the SMA wire jacketed concrete exhibited a slight increase in bond stress after cracking, while plain concrete experienced a sharp decrease. The confined concrete contracted after the stable region, while plain concrete continued to expand. The confined concrete showed radial cracks, indicating a change in bond failure mode from splitting to pull out. The SMA wire jackets shifted the bond failure mode without providing composite behavior with concrete under tension or compression.

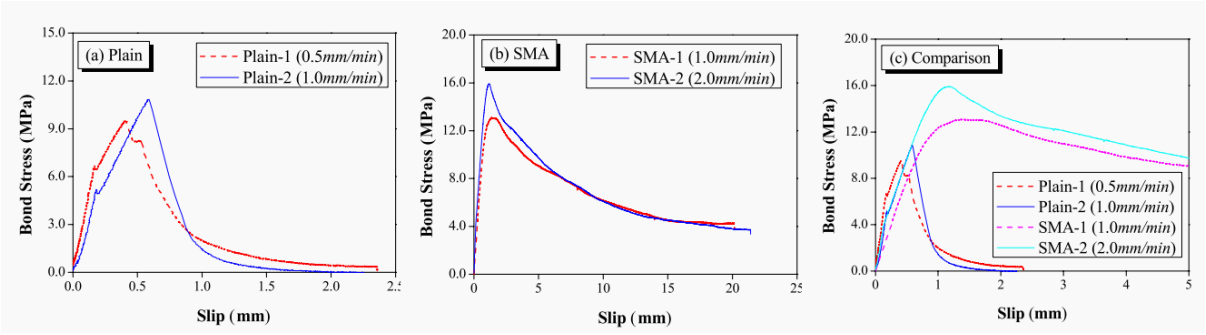

Figure 2.17 - Comparison of slip according to bond stress (Choi et al., 2010)

Choi et al. (2018) investigated the impact of different fiber-end shapes on the pullout resistance of NiTi superelastic SMA fibers. The study utilized four end shapes (straight-end, L-shape, N-shape, and crimped end) and performed hysteretic pullout tests using single-fiber specimens. The findings indicated that the L-shape ended fiber did not exhibit superelastic behavior and remained within the elastic range. The N-shaped fiber experienced stress concentration on the bent part, preventing the occurrence of flag-shaped behavior which is shown in **Figure 2.18** and **Figure 2.19** shows the pull out behavior of straight fibers which is very less than others.

However, the crimped-ended SMA fiber demonstrated superelastic behavior and achieved flag-shaped behavior, showcasing self-centering capacity. Fiber slip was observed, suggesting the need for further research on smaller cross-sectional area fibers, lower upper plateau stress values, and heating methods to achieve ideal flag-shaped behavior and prevent fiber slipping. Notably, heating was found to enhance deflection recovery in N-shaped SMA fibers.

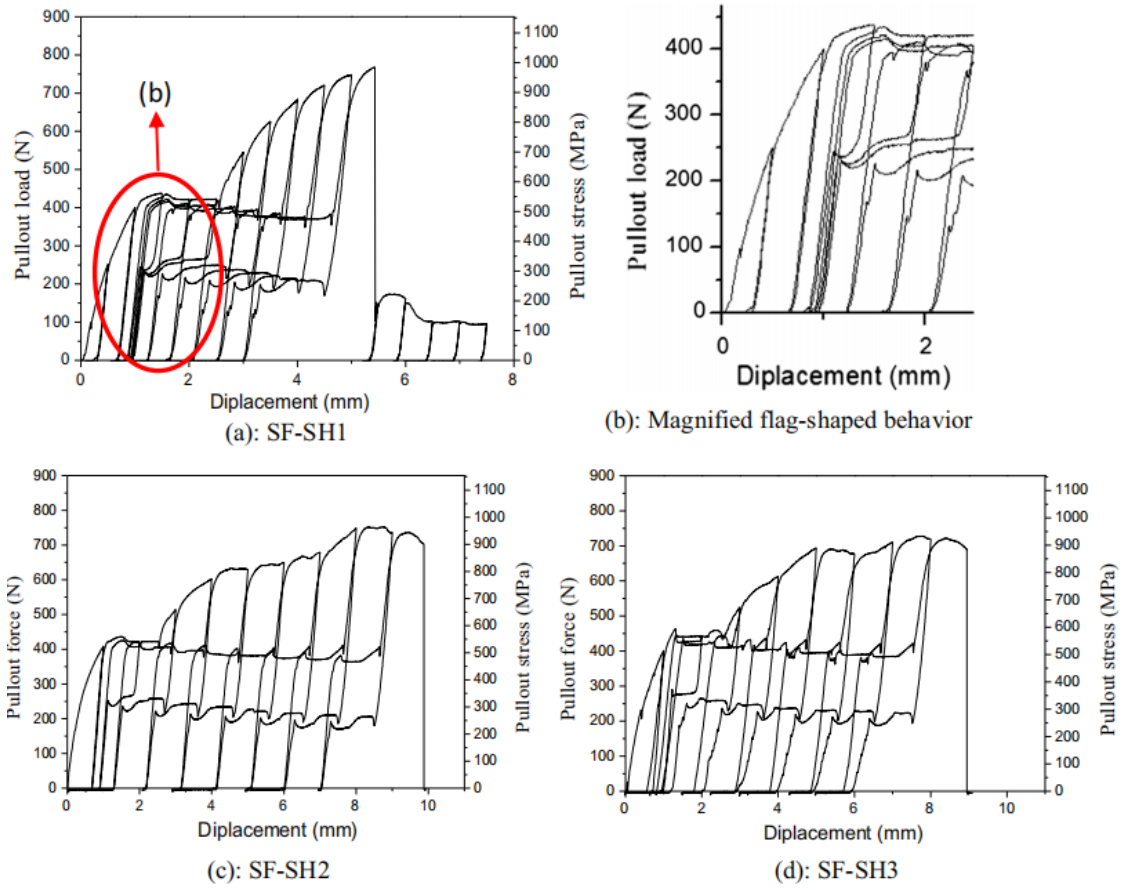

Figure 2.18 Pull out behavior of SMA hooked Fibers (Choi et al., 2018)

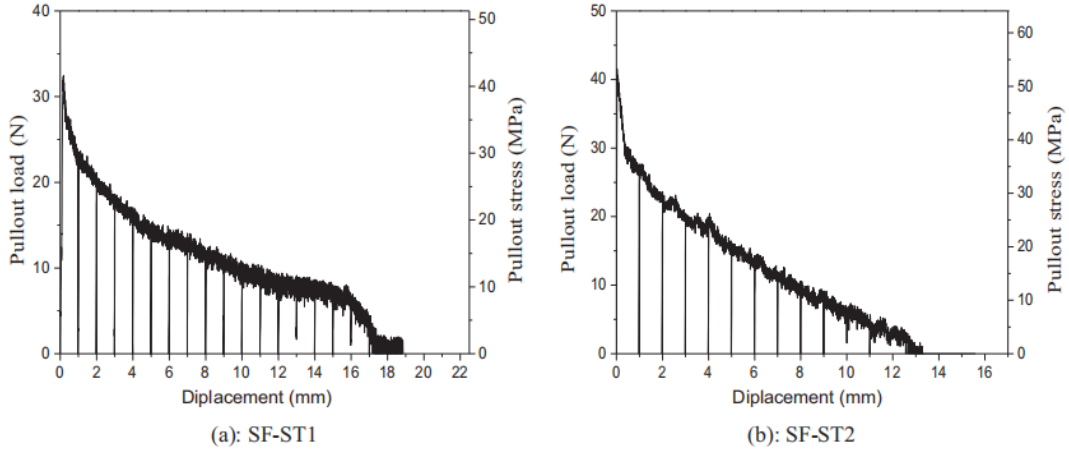

Figure 2.19 Pull out behavior of SMA straight Fibers (Choi et al., 2018)

2.5 PARAMETERS AFFECTING THE BOND STRENGTH

Choi et al. (2023) conducted pullout tests on concrete specimens with cold-drawn SMA crimped fibers to investigate their bond behavior under various conditions. The effects of temperature, mix design, and cracking patterns were considered. The bond stress and slip relationships for plain and SMA crimped fiber specimens were compared, and the radial strains were observed. The results showed that non-heating SMA crimped fiber specimens exhibited passive bond behavior similar to steel fibers, while heated SMA fiber-reinforced concrete displayed more ductile behavior. The bond strength increased with higher SMA fiber volume fractions, and heated specimens exhibited moderate confinement behavior. The radial strains varied depending on temperature and volume fraction, with some discrepancies observed. The study suggests formulating bond strength predictions for concrete with SMA crimped fibers, considering factors such as volume fraction, temperature, and recovery stress. Future research should investigate a wider range of volume fractions, cover-to-bar diameter ratios, and the effects of high temperature on bar deformation.

Dehghani et al. (2022) examined the pullout behavior of superelastic shape memory alloy (SMA) fibers and steel fibers in self-compacting concrete. The variables considered were the type of hooked-ends, embedded length, and loading rate. The experimental results showed that SMA fibers experienced higher slip before reaching peak pullout load compared to steel fibers. The slip of straight fibers, both SMA and steel, was sensitive to loading rate, while most hooked-end fibers exhibited rate insensitivity. SMA fibers with hooked-end type H3 exhibited the highest pullout strength and induced tensile stress. The study also found that steel fibers exhibited higher pullout resistance than SMA fibers due to a broader contact area with the matrix. Changing the type of hooked-end enhanced the mechanical bond and pullout energy. SMA fibers were found to be independent of loading rate, while steel fibers exhibited rate sensitivity. The surface micro-topography of steel fibers showed extensive matrix damage, whereas SMA fibers exhibited insignificant damage.

Rodino et al. (2022) investigated the static and cyclic pullout behavior of SMA-polymer samples. The static pullout strength under mechanical load was found to be significantly higher than the stress required for martensite reorientation and close to the maximum recoverable stress of SMA wires. The static pullout stress was largely unaffected by cyclic activation cycles and comparable to that of manufactured samples. However, a notable reduction in pullout stress was observed when combining mechanical load with SMA thermal activation, attributed to interface stresses from both load and shape recovery, along with a decrease in polymer strength

at higher temperatures. The fatigue strength of the SMA-polymer system, even after 5000 cycles, remained higher than the stress required for martensite reorientation, indicating its suitability for repeated activations of morphable surfaces.

Choi et al. (2020) studied the stress distribution on crimped shape memory alloy (SMA) fibers during pullout tests was investigated through experimental tests and finite element (FE) analyses. The crimped fibers had different diameters but the same wave depth and length. The results revealed that the crimped fiber with a larger diameter exhibited greater peak pullout stresses. The stress distribution varied between the concave belly side of the fiber and the mortar matrix. The embedded portion of the crimped fiber experienced peak stress when the fiber passed through the mortar valley, with deeper embedded wave elements experiencing higher peak stresses. The fiber direction and pullout force influenced the peak stress, and the stress distribution in the embedded portion differed from that of the free portion of the fiber. The stretching effect reduced as the distance from the summit point increased, resulting in a decrease in pullout stress.

Abdallah et al. (2018) studied the bond between fiber and matrix is critical for transmitting stresses in composites. Understanding the fiber-matrix interface mechanics is crucial for assessing the tensile behavior of fiber-reinforced composites (SFRC). Pullout resistance of fibers significantly impacts the composite's mechanical properties. Straight fibers rely on friction and adhesion, while hooked-end fibers benefit from mechanical interlocking which can be seen in **Figure 2.20.**

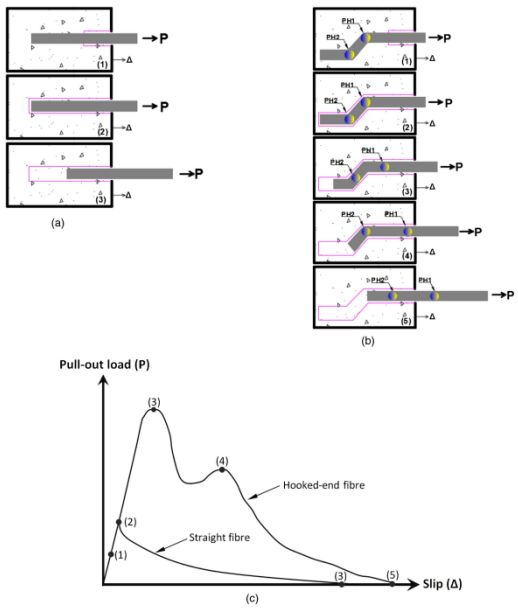

Figure 2.20 Pullout behavior of straight fiber (Stages 1–3) and hooked-end fiber (Stages 1–5) (Abdallah et al., 2018)

Kim et al. (2015) investigated pullout resistances of deformed shape memory alloy (SMA) fibers in cement mortar. Deformed geometries, including dog bone–shaped and end-deformed, showed higher pullout resistances compared to the smooth geometry. The NiTiNb alloy fibers with deformed geometries had stronger bond strengths than NiTi alloy fibers with deformed geometries, while NiTi alloy fibers with smooth geometry had higher bond strength than NiTiNb alloy fibers with smooth geometry. Heat treatment had a greater impact on the pullout resistance enhancement of the NiTi alloy than the NiTiNb alloy. The dog bone–shaped geometry exhibited the highest strength ratios in both maximum load and equivalent load after heat treatment.

Baena et al. (2009) investigated the interfacial bond behavior between carbon and glass fiber reinforced polymer (FRP) bars and two concrete strengths. They found that bond behavior is influenced by factors like concrete compressive strength, rebar diameter, and surface treatment. Changes in concrete strength affected bond strength and failure mode. Surface treatment exhibited different bond mechanisms, particularly in high-strength concrete. Rebar geometry, represented by as and CLR ratios, influenced bond strength, with higher values leading to stronger bonds. Larger rebar diameters resulted in lower bond strength, especially in high-strength concrete. The initial stiffness was unaffected by rebar diameter, but varied with concrete compressive strength for some GFRP rebars. Slip values were higher for GFRP bars compared to CFRP bars, and the bond-slip behavior differed between steel and FRP rebars. Analytical models were calibrated with new diameter-dependent equations, resulting in improved agreement with experimental data.

Markovich et al., (2003) tested various conventional and fiber reinforced mortars to evaluate their workability, strength properties, and single fiber pullout behavior. The findings indicated that mortars with lower water/cement ratios demonstrated better overall performance. The inclusion of 4% volume of short fibers improved material performance, especially in mortars with a water/cement ratio of 0.40, leading to a 40% increase in the average single fiber pullout force. Microstructural observations revealed that short fibers acted as bridges, mitigating micro cracking around the fiber during pullout and enhancing the overall response. However, the addition of 2% volume of longer fibers did not yield further improvements, potentially due to unsatisfactory workability and increased porosity. It was also noted that further modifications to mortars with lower water/cement ratios and additional fibers may lead to fiber fracture, emphasizing the suitability of larger fibers in such mixtures.

2.6 BOND STRENGTH AFFECT BY HEATING OF SAMPLE

Haddad and Shannis (2004) examined the behavior of high strength concrete (HSC) with natural pozzolana and reinforcing steel after a fire incident. Specimens were prepared and cured in water at 23℃ for 40 days before being exposed to temperatures of 600℃ and 800℃. The researchers also evaluated the extent of post-fire cracking on the surface of pullout specimens. Based on the obtained results, empirical models were developed to predict the percentage reduction in bond strength. The findings revealed that there was a 24% reduction in bond strength at 600℃ and a significant 74% reduction at 800℃. The use of natural pozzolana in HSC had a negative impact on the cementing value, which outweighed the benefits of reduced cracking. Additionally, the HSC pullout specimens that underwent heat treatment exhibited higher slippage values upon failure compared to the untreated specimens. Moreover, as the temperature increased to 800℃, the bond strength experienced further reduction, while the contribution of natural pozzolana remained unchanged.

Table 2.2 Compressive and splitting tensile strengths for HSC at different temperatures (Haddad and Shannis, 2004)

NP content %	**Compressive Strength (MPa)**			**Splitting Tensile Strength (MPa)**		
	23℃	**600℃**	**800℃**	**23℃**	**600℃**	**800℃**
0	73.15	44.24 (39.52%)	24.47 (66.55%)	4.87	3.79 (22.23%)	2.82 (42.18%)
10	65.95	40.08 (39.23%)	17.26 (73.83%)	4.62	3.61 (22.05%)	2.37 (48.84%)
15	66.97	39.66 (40.78%)	16.67 (75.11%)	4.66	3.59 (23.04%)	2.37 (50.11%)

Table 2.3 Bond strength, critical bond stress, and free-end-slip at failure for HSC before and after exposure to heating (Haddad & Shannis, 2004)

NP content %	Bond Strength (KPa)			Critical bond stress (MPa)		
	23℃	600℃	800℃	23℃	600℃	800℃
0	4016.5	3459.2 (14.8 %)	1900.1 (47.1 %)	2225	91.9 (95.9%)	246.6 (88.9 %)
10	3763	2947.7 (21.7 %)	2056.3 (54.7%)	3276.1	102.1 (96.9%)	127.1 (96%)
15	3670.2	2910.9 (20.7%)	1357.9 (63.0%)	3344.5	8.3 (99.8 %)	22.6 (99.3%)

Lubloy et al. (2014) studied the bond behavior between concrete and reinforcing bars under elevated temperatures was investigated. Five different concrete specimens were prepared and subjected to various maximum temperatures, including 20°C, 150°C, 300°C, 400°C, 500°C, and 800°C. After heating the specimens for two hours, they were cooled down and then tested for pull-out strength at room temperature. To assess the compressive strength, standard cubes were also cast, cured, heat-treated, and tested. The results indicated a reduction in residual compressive strength as the temperature increased, and the bond stress-slip behavior underwent changes under high temperatures**.**

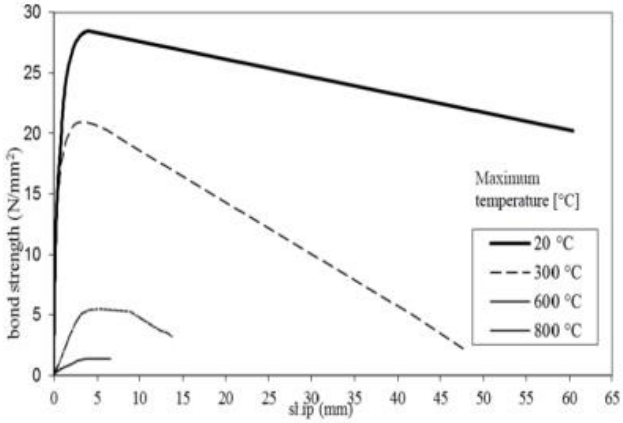

Figure 2.21 The τ_b vs slip diagram as a function of temperature (Lubloy et al., 2014)

Khalaf and Huang (2016) developed a model to predict the average bond stress-slip relationship between prestressed steel strands and concrete in prestressed concrete structures. The model takes into account the mechanical interlocking between the strands and the surrounding concrete, considering factors such as variations in concrete properties, strand

geometries, and the type of strand surface. It also considers the degradation of materials and bond characteristics at elevated temperatures, which are related to changes in concrete material properties with temperature. The developed bond stress-slip model was incorporated into a two-node bond-link element within the Vulcan software, allowing for the analysis of the structural behavior of prestressed concrete members in fire conditions. The proposed model was validated against previous experimental results at both ambient and elevated temperatures.

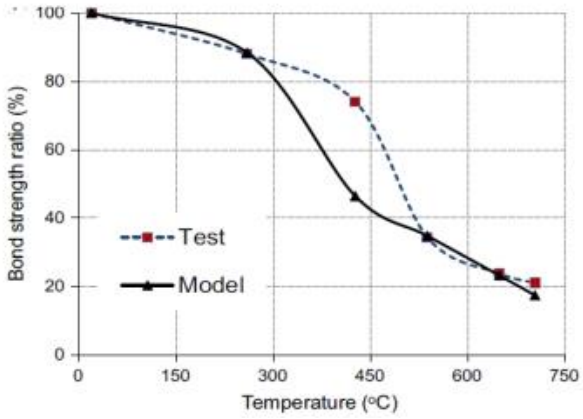

Figure 2.22 Comparison of predicted and tested bond strength degradation with concrete compressive strength of 98.8 MPa at elevated temperatures (Khalaf & Huang, 2016)

CHAPTER 3

EXPERIMENTAL PROGRAM

3.1 GENERAL

This chapter explains the materials utilised in the experimental program, the design compositions of the experimental samples, and the technique used to execute the experiments. The first section discusses the materials needed to make the concrete, their physical qualities, and their chemical compositions. The next part discusses concrete mix quantities, design compositions, mixing techniques, and wet concrete qualities. The following sections describe the experimental setup, tests used, and reference codes used in the testing procedure. The testing approach has only been categorized as mechanical strength.

3.2 MATERIALS USED IN THE STUDY

The binder materials used in the present study are Ordinary Portland Cement **(53 grade)**, conforming to IS12269 (BIS 1987), Crushed basalt used as coarse aggregate sand as fine aggregate, Master glenium as admixture and Shape Memory Alloy (SMA) as fibers.

3.2.1 Cement

Cement is one of the best binding materials used in concrete. As per availability, cement from two different manufacturing industry were initially used in the present study for Ordinary Portland cement of 53 grade**,** namely, Wonder cement and Ambuja (Powercem) Cement conforming to IS12269 (BIS 1987). The cement bags were collected from a single lot and used for preparing concrete mixes. The cement samples were collected and tested according to the guidelines of IS: 4031 (Part 11):1988, IS: 4031(Part 5): 1988, and IS: 4031 (Part 6): 1988 (IS4031 (BIS 1988a; BIS 1988b; BIS 1988c)). The properties of the cement investigated were specific- gravity, initial setting time, consistency, etc. The physical properties of the cement are presented in **Table 3.1.**

Table 3.1. Physical properties of the cement

Properties of OPC-53	**Wonder Cement**	**Ambuja (powercem)**
Specific Gravity	3.12	3.14
Consistency of standard cement paste (%)	30	32
Initial-Setting Time (min)	160	135
Final - Setting Time (min)	210	200

3.2.2 Aggregates

Aggregates fill the maximum volume of the concrete and are assumed to have a high impact on the properties of concrete. The aggregates should be in proper shape and size, clean, hard, and well-graded. Based on the size of the particle, the aggregates are divided into two groups.

- Fine aggregates: The particle size is less than 4.75 mm and (Fig. 3.1a).
- Coarse aggregates: The particle size is greater than 4.75 mm and less than 12.5 mm (Fig. 3.1b).

(a) (b)

Figure 3.1. (a) Fine Aggregate of size less than 4.75 mm, (b) Coarse aggregates of size less than 12.5 mm and greater than 4.75 mm.

3.2.2.1 Fine aggregates

Locally procured river sand was used as fine aggregates. The Particle Size Distribution (Sieve analysis) and other physical properties of the fine aggregates are presented in **Table 3.2** and **Table 3.3** respectively. The Sand was first sieved through a 4.75 mm sieve to remove any particles greater than 4.75 mm and then washed to remove the dust. The fine aggregates were tested as per Indian Standard Specifications IS 383 (BIS 1970). Based on Particle Size distribution, the fine aggregates fall under Zone II of IS 383 (BIS 1970).

Table 3.2 Sieve analysis of fine aggregates

IS Sieve	Weight retained (gm)	Percentage weight retained	Cumulative % of weight retained	Cumulative % of weight passing	Limit by IS 383 for Zone -II
4.75 mm	14	1.4	1.4	98.6	90 to 100
2.36 mm	11	1.1	2.5	97.5	75 to 100
1.18 mm	386	38.6	41.1	58.9	55 to 90
600 µm	172	17.2	58.3	41.7	35 to 59
300 µm	266	26.6	84.9	15.1	8 to 30
150 µm	120	12	96.9	3.1	0 to 10
Pan	31	3.1	-	-	
Total	1000	100	285.1		
Fineness Modulus	= 285.1/100	= 2.851			**Hence, Zone - II**

Table 3.3 Physical properties of fine aggregates

Characteristics	Obtained Results	Requirements as per IS 383:1970
Grading	Zone - II	Zone - II
Fineness Modulus	2.851	2.0 to 3.5
Weight of saturated sand, A (gm)	500	
Weight of pycnometer with sand, B (gm)	1831	
Weight of pycnometer with Water, C (gm)	1519	
Weight of oven dry aggregate, D (gm)	553	
Specific gravity =(A/[A-(B-C)]) =	2.688	2.6 to 2.7
Weight of saturated sand A* (gm)	997	
Weight of oven dry sand, B* (gm)	982	
Water absorption = (B*- A*)/ (A*) =	1.5%	

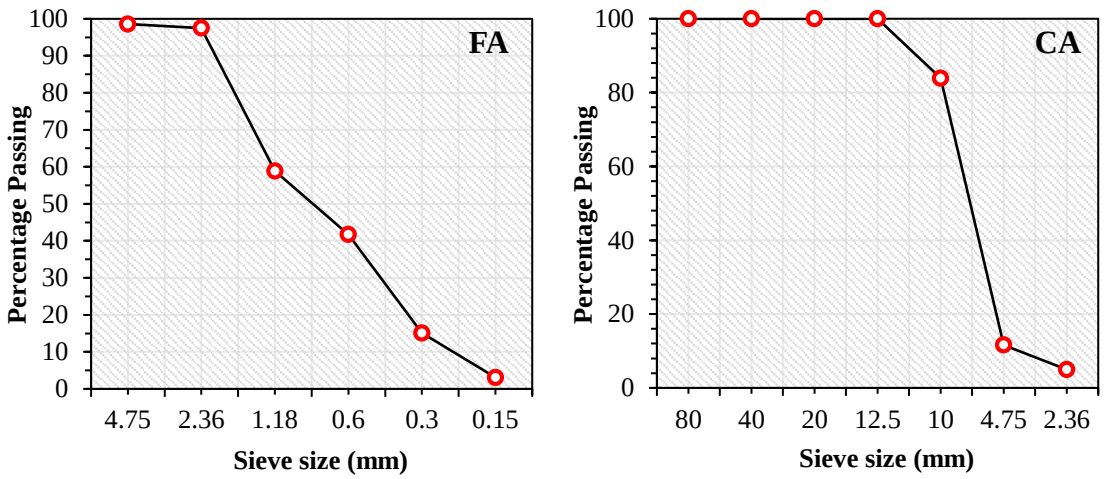

(a) (b)

Figure 3.2. Particle size distribution of (a) Fine aggregates; (b) Coarse aggregates of 10 mm

3.2.2.2 Coarse aggregates

Crushed stone aggregates size (locally available) of more than 4.75 mm and less than 12.5 mm are used throughout the experimental study. The particle size distribution of coarse aggregate is given in **Table 3.4.**

Table 3.4 Sieve analysis of 10 mm aggregates

I.S. Sieve	Weight retained (gm)	Percentage of weight Retained	Cumulative Percentage of weight Retained	Cumulative percentage of weight passing	Limit by IS 383
80 mm	0	0	0	100	
40 mm	0	0	0	100	
20 mm	0	0	0	100	
12.5 mm	0	0	0	100	100
10 mm	804	17.28	16.08	83.92	85 to 100
4.75 mm	3615	72.30	88.38	11.62	0 to 20
2.36 mm	332	6.64	95.02	4.98	0 to 5
Pan	249	4.98	_	_	_
Total	5000	100	199.48		
Fineness modulus =	(199.48 + 400)/100 =	5.9948	6.		

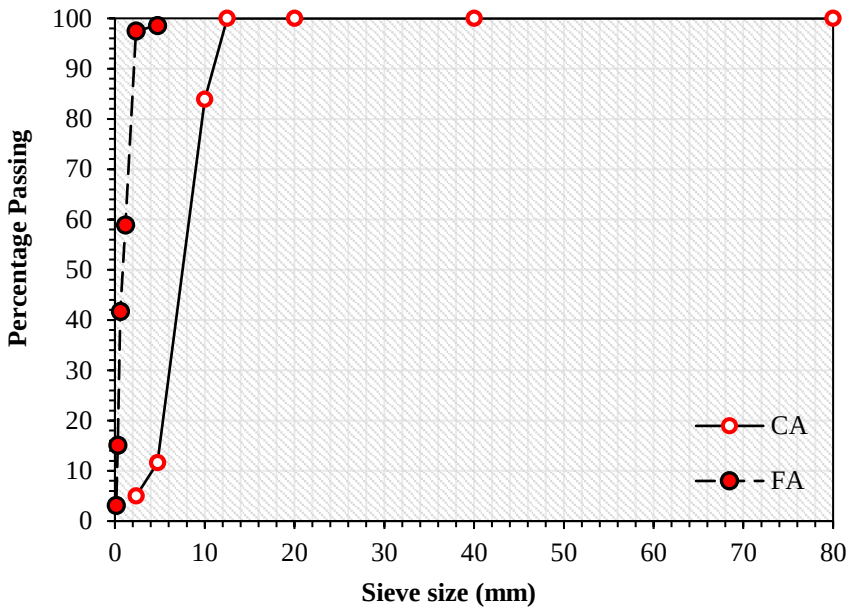

Figure 3.3- Particle size distribution comparison graph of FA and CA

3.2.3 Water

Water is a necessary component of the concrete mix. The water used to mix and cure concrete should be devoid of any potentially dangerous elements. Water should be devoid of organic matter, silt, oil, sugar, chloride, and acidic stuff. As a result, potable water is typically used for this purpose. During the whole casting and curing process, potable tap water was used which is maintained at a constant temperature of 27°C.

3.2.4 Superplasticizer

A water-reducing superplasticizer is necessary for good workability. They are polymers that dissolve in water to generate lengthy molecules with large negative charges. The combined water between the cement agglomerations is liberated and considerably enhances the workability of concrete as the cement particles are separated by electrical repulsion between these negative charges. In the current investigation, a polycarboxylate ether-based superplasticizer complying with IS 9103(BIS 1999) was used in the admixture. It is also referred to as the "new generation of high-performance concrete admixture." It is a good-performing water-reducing chemical that combines water reduction, slump prevention, strengthening, shrinkage, and environmental protection. It is also an excellent additive to produce high-strength materials. Superplasticizer mixed with water and changes of color is shown in **Figure 3.4** and the properties of superplasticizer is described in **Table 3.5**.

Figure 3.4. Superplasticizer mixing with water

Table 3.5 Properties of superplasticizer (Master Glenium 51 Datasheet)

Parameter	**Master Glenium 51**
Type	Liquid
Appearance	Reddish Brown
PH	≥ 6
Chloride content (%)	< 0.2
Water reducing ratio (%)	> 25

3.3 CONCRETE MIX PROPORTION

3.3.1 Trial 1: Using premix concrete (Mapei make)

Mapei is a global company specializing in the production of chemical products for the construction industry. Founded in 1937 in Milan, Italy, Mapei has become a leading manufacturer of adhesives, sealants, and chemical solutions for building and infrastructure projects. Their extensive product range includes adhesives for tiles and stone, grouts, waterproofing systems, concrete additives, and solutions for the restoration and preservation of historical buildings. Mapei operates in over 90 countries, utilizing a network of subsidiaries, production facilities, and research centers to provide innovative and sustainable construction solutions to professionals worldwide.

3.3.1.1 Preparation of the mortar

To prepare a mix using Mapefill 05, follow these steps: Start by pouring 3.5 liters of water into a concrete mixer. Then, turn on the mixer and gradually add the Mapefill 05 while the mixer is running. Mix the ingredients for 1-2 minutes, ensuring that all the powder is incorporated. If there are any unmixed powder particles sticking to the sides of the mixer, scrape them off and

continue mixing for another 2-3 minutes until the mixture becomes fluid and free from lumps. It's important to avoid introducing excessive air into the mix during stirring.

For smaller quantities, a mortar mixer or a drilling machine with a stirrer attachment can be used. However, manual mixing should be limited to exceptional circumstances, as it requires more water, which can negatively affect the characteristics of Mapefill 05, such as mechanical strength and shrinkage. To ensure the effectiveness of the product, suitable reinforcement or formwork should be in place to counteract the expansion forces. The expansion phase occurs during the initial days of curing. There is some difference in the products of Mapei, which is shown below in **Table 3.6**.

Table 3.6 – Difference between Mapefill 05 and Mapefill 08.

Product Identity	**Mapefill 05**	**Mapefill 08**
Type	Powder	Powder
Maximum aggregate dia.(mm)	6	10
Dry solid content (%)	100	100
Colour of the mix	Grey	Grey
Mixing ratio	25 kg bag of Mapefill 05 with 3.5 litres of water	100 parts of Mapefill 08 with 10-11 parts of water and 0.16-0.32% of Mapecure SRA
Consistency of the mix	Fluid	Fluid
Density of the mix (kg/m3)	2200 ± 50	2300
Ph of the mix	>12	>12.5
Pot life at 23°c and 50% R.H.	15 minutes.	Approx 1 hr.
Compressive strength	After 1 day > 10 After 7 days > 40 After 28 days > 50	After 1 day > 15 After 7 days > 50 After 28 days > 70

Premix was first used to achieve the required compressive strength, i.e. ≥ 60 MPa. Mapefill 05 premix was firstly cast with 0.11, 0.13 and then 0.14 water-cement ratio. Three experiments were undertaken on the cube of sample size 100 mm with varying w/c ratios. The elaborated mix proportions are given below in **Table 3.7.**

Table 3.7. Mix proportion of premix.

Description	**Mix 1**	**Mix 2**	**Mix 3**
Type of concrete	Premix concrete	Premix concrete	Premix concrete
Brand name	Mapefill 05	Mapefill 05	Mapefill 05
W/c	0.11	0.13	0.14
Cube compressive strength in MPa (after 7 days)	_	_	47.2
Cube Compressive Strength in MPa (after 28 days)	46.65	45.2	57.67
Conclusion	Not Suitable (≤ 60 MPa)	Not Suitable (≤ 60 MPa)	Not Suitable (≤ 60 MPa)

In conclusion, the compressive strength testing of the sample has resulted in achieving a strength of 57 MPa, which is slightly below the target strength of 60 MPa. While the material exhibited considerable strength, it fell short of meeting the specific desired requirement. So it is **not suitable** for the project.

3.3.1.2 Flow table test (workability test for small aggregate size)

The flow table test is a common method used to assess the workability of concrete. A circular metal table is placed horizontally with base diameter 300 mm and a slump cone having top diameter 70 mm, bottom diameter 80 mm, and height 40 mm is shown in **Figure 3.5** and it is filled with freshly mixed concrete is placed at the centre of the table. After concrete was poured in cone and then it received 25 tamping for the concrete to settle down. After that the cone is carefully lifted, allowing the concrete to flow outward and spread across the table due to its own weight. The diameter of the concrete spread on the table is measured, indicating the flow or spreadability of the concrete mixture which is shown in **Figure 3.6**. This test helps in determining the consistency and workability of concrete, aiding in quality control and ensuring proper placement on construction sites.

Figure 3.5 Flow table Instrument (a) Side view of flow table; (b) Top view of flow table; (c) Flow of concrete measurements

A flow value of 130 mm indicates that the concrete mixture has a relatively high workability, meaning it is highly fluid and easy to place and compact. The flow value is typically measured using a standardized test method, such as the slump test or the flow table test.

3.3.2 Trial 2: Mix design for /Ultra-High Strength Concrete (UHSC) of M113.

According to the **American Concrete Institute (ACI) code**, UHSC is typically defined as concrete with a specified compressive strength greater than 150 MPa (22,000 psi). The ACI defines this strength range as "very high strength concrete" or "high-performance concrete." **Euro code specifically Euro code 2 (EN 1992-1-1),** defines UHSC as concrete with a characteristic compressive strength greater than 120 MPa (17,400 psi).

Ultra-high-strength concrete (UHSC) is a groundbreaking construction material that has revolutionized the field. With an incredibly high compressive strength exceeding 150 MPa, UHSC surpasses the strength of conventional concrete through precise material selection and proportions. Its compact microstructure and reduced water-to-cement ratio contribute to improved resistance against cracking, corrosion, and impact.

The reference for the mix design in the present study has been taken from **Jiang du et al., (2021)** and mix proportions is shown below in **Table 3.8.**

Table 3.8 Mix proportion for ultra-high strength concrete.

Description	**Mix design (M113)**
Cement type	OPC 53 (wonder)
Cement (kg/m^3)	675
W/C	0.2
Coarse aggregate (Kg/m^3)	576.3
Fine aggregate (kg/m^3)	865.5
Silica fume	45
Limestone powder	180
Fly Ash	_
Flow table	120 mm
Superplasticizer (%)	1.2% by weight of binder
Cube compressive strength (after 7 days)	29.92 MPa
Cube Compressive Strength (after 28 days)	41.5 MPa
Conclusion	Not Suitable (≤ 60 MPa)

We can conclude that the compressive strength results of the sample have fallen significantly short of the target strength of 113 MPa, reaching only 41.5 MPa. This substantial disparity between the desired and achieved strength indicates a considerable performance gap in the material's properties. So, it is **not suitable** for this project.

3.3.3 Trial 3: Design mix proportions of concrete for target strength M60.

High strength concrete (HSC) may be defined as concrete with a specified characteristic cube strength between 60 and 100 N/mm^2, although higher strengths have been achieved and used. The proportions of concrete components such as cement, sand, aggregates, and water are referred to as concrete mix ratios. The mix ratios are determined by the type of building and the mix designs. The M60 mix was developed with a w/c of 0.29 and prepared utilizing the qualities of materials listed above according to the technique given in IS 10262(BIS 2019). Many tests were carried out prior to the finalization of the mix designs. As shown in **Table 3.9**, two experiments were undertaken on the cube of sample size 100 mm with varying w/c ratios

with and without superplasticizer. The process from mixing to casting is shown in **Figure 3.6**. Compressive strength test of M60 mix design at different testing ages (days) is shown in **Figure 3.7, 3.8 and 3.9**.

Table 3.9 Concrete mix proportions for trials.

Description	**Mix Design (M60)**
Cement type	OPC 53 (Ambuja Powercem)
Cement (kg/m^3)	550
W/c	0.29
Coarse aggregate (Kg/m^3)	915
Fine aggregate (kg/m^3)	907.24
Silica fume (Kg/m^3)	-
Fly Ash (kg)	-
Flow table	> 100 mm (slump cone test)
Superplasticizer (%)	1.2% by weight of cement
Compressive strength (@ 7 days)	46.12 MPa
Compressive Strength (@ 28 days)	60.2
Compressive strength (@ 56 days)	62 MPa
Conclusion	Suitable ($\geq$ 60 MPa)

The testing of cubes at 7, 28 and 56 days in **Figure 3.7, 3.8** and **3.9** clearly shows the compressive strength testing of the sample has been successful, as the achieved strength is 60.2 MPa surpassed the target strength of 60 MPa. This outcome demonstrates the material's capability to meet and even exceed the desired compressive strength requirement.

(a)

(b)

(c)

(d)

(e)

Figure 3.6 Preparation of concrete specimens for pull-out test - (a) Mixing; (b) Batching; (c) Casting; (d) Process of embedment of fiber in a concrete; (e) After finishing

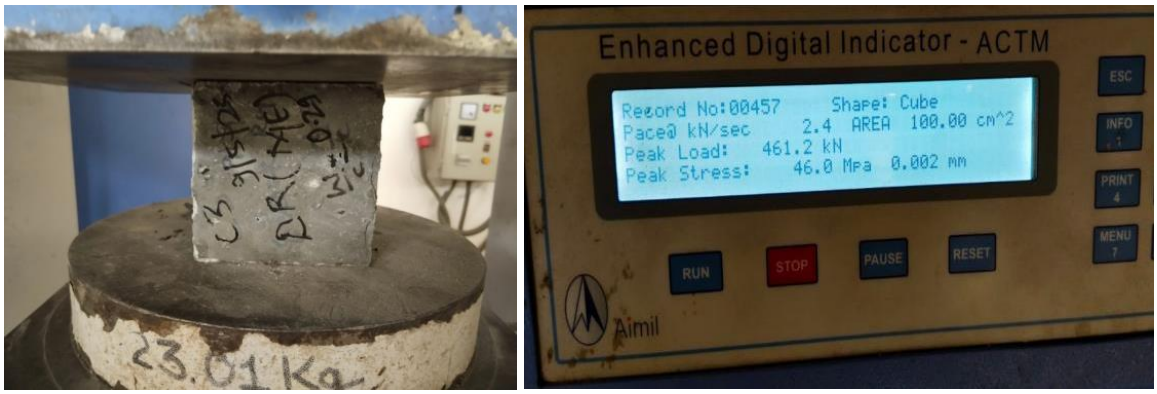

Figure 3.7 Testing of cubes and its strength after 7 days of Mix Design (M60)

Figure 3.8 Testing of cubes and its strength after 28 days of Mix Design (M60)

Figure 3.9 Testing of cubes and its strength after 56 days of Mix Design (M60)

Following the completion of the trials, the mix is finalized for casting based on the workability and strength characteristics, as given in **table 3.10**.

Table 3.10 Finalized concrete mix design proportions

Mix	**Proportion**
Cement (kg/m^3)	550
Fine aggregate (kg/m^3)	907.24
Coarse aggregate (kg/m^3)	915
water (kg/m^3)	159.5
Superplasticizer (%)	1.2% by weight of cement

The concrete was cast after the mix design was finalized. Mixes were prepared by keeping the cement content, Fine aggregate, Coarse aggregate, and water content constant in all mixes. The mix proportions of the ingredients are mentioned in **Table 3.11**.

Table 3.11 Mix proportions of Ingredients (M60)

Cement	**Fine Aggregate**	**Coarse Aggregate**	**Water**	**Superplasticizer (% by wt. of cement)**
1	1.65	1.66	0.29	1.2

3.3.3.1 Moulding of SMA fibers

The process of embedding specially shaped Shape Memory Alloy (SMA) fibers in concrete required the use of a hand-held die. Two separate dies were created, one for producing crimped fibers and another for producing hooked-end fibers. These dies were used to change the shape of linear SMA fibers into the desired crimped or hooked-end shapes.

The die for hooked-end fibers had a U-shaped design with a 25 mm trough, a 20 mm crest on both sides, a 10 mm height, and a total length of 65 mm. This shape is depicted in **Figure 3.10**. By applying force with the hand, the SMA fibers were transformed into the hooked-end shape, as shown in **Figure 3.11**. On the other hand, **Figure 3.12** illustrates the shape of straight SMA fibers without any modifications.

In order to ensure proper embedment of the fibers in the concrete, the desired embedment length was marked, as demonstrated in **Figure 3.13**.

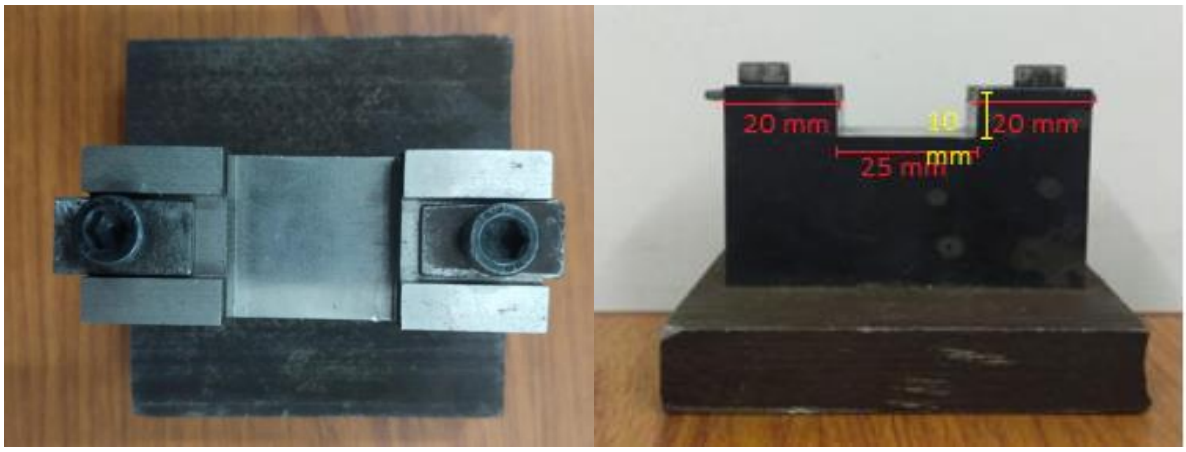

(a) (b)

Figure 3.10 Die for hooked end shape – (a) Top view, (b) Elevation

(a) (b)

(c) (d)

Figure 3.11 Shape of hooked end shape; (a) Length of Hooked SMA; (b) Crest length of Hooked SMA; (c) Slope of Hooked SMA; (d) Diameter of Hooked SMA

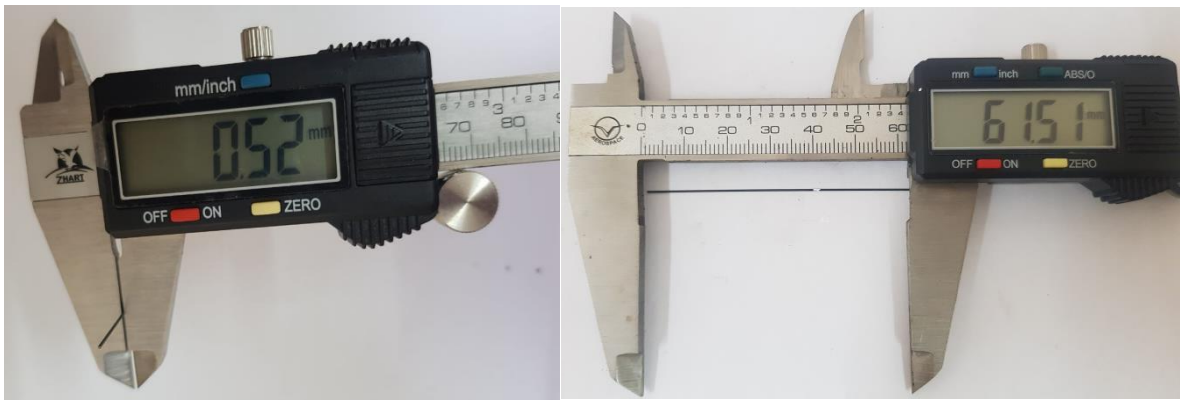

(a) (b)

Figure 3.12 Shape of Straight end shape (a) Length of Straight SMA; (b) Length of Straight SMA

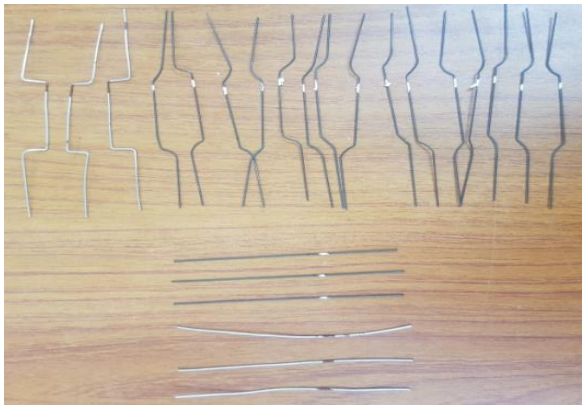

Figure 3.13 Embedding length marked on SMA fibre

3.4 MIXING PROCEDURE AND CURING METHODOLOGY

The ingredients of concrete were thoroughly mixed with the help of a rotary mixer to achieve a uniform mix. In the beginning, drying mixing was done until a uniform blend was obtained. The water incorporated with the superplasticizer was added in phase wise manner. The total mixing time was about 2-3 minutes. Before concrete placement in moulds, various tests were performed for each mix on freshly hydrating concrete. A vibrating table was used to compact the moulds. After compacting the moulds 40mm of hooked and crimped shapes of NiTinol wire are embedded in the moulds. The specimen of size of 100 mm was cast as per the testing methodology requirements. All the specimens were kept in moulds for 24 hours and then removed from moulds to be kept for curing. After demoulding and marking the samples, they were cured in water for 28 days. The curing of samples was done in a curing tank which is shown in **Figure 3.14**. Curing should be done with extreme caution to ensure that the concrete specimens achieve the requisite strength. If curing is not done properly, the concrete may lose moisture and hence be unable to acquire the appropriate strength. After the curing period of 28

days, the respective samples were removed from the curing tank for tests determining the mechanical properties and bond test.

Figure 3.14 - Curing of samples in Curing tank

3.4.1 Testing of Casted Concrete Specimens

The different tests are performed on the casted specimens and standard followed for the testing procedures are given below:

Table 3.12 Tests performed and codes followed

Test	code
Compressive strength test	IS: 516-1959
Pull out test	IS: 2770- 1967 (part 1)

Table 3.13 Type and size of specimen for various tests performed

Name of the test	Type of specimen	Size of specimen (mm)
Compressive strength	cube	100×100×100
Pull out test	cube	100×100×100

The test setup for workability and mechanical properties of concrete are discussed below:

3.4.2 Workability of concrete

The workability of concrete refers to its ability to be easily manipulated and moulded during construction. A properly workable concrete mix ensures efficient placement and compaction. Factors such as water-cement ratio, aggregate gradation, and chemical admixtures influence

workability. An ideal workable concrete blend promotes smooth pouring, levelling, and finishing, facilitating construction tasks.

3.4.3 Slump Cone Test

The slump cone test is one of the most accessible and popular tests used to determine that workability of the mix. The test was conducted as per IS 1199 Part 2 (BIS 2018), as shown in **Figure 3.15**. For conducting the test, a slump cone of an internal diameter of the slump cone at top is 10 cm and at bottom, it is 20 cm with the height of the slump cone 30 cm. The mould is placed on a horizontal and rigid surface. Mould was then filled in 3 layers with 25 tamping to each layer. Mould was slowly raised in a vertical direction and concrete was allowed to subside. The difference in levels between the height of the mould and that of the highest point of the subsided concrete was measured in mm and it was taken as the slump value of the mix.

Figure 3.15 Slump measurement of concrete

3.4.4 Mechanical properties

Compressive strength is the maximum compressive stress that a given solid material can sustain without fracture under a gradually applied load. This test was performed in accordance with IS 516 (BIS 1959). The cubes are placed in such a way that the application of load is done to the opposite sides of the cubes as cast where the casting face and the testing faces are perpendicular to each other. The load is axially applied without any shock and increases continuously at a loading rate **2.4 KN/s**. The maximum load sustained by the specimen is recorded and divided by cross-sectional area to obtain the compressive strength of the specimen.

Concrete cubes of 100×100×100 mm dimension were casted to test for compressive strength and tested as specified in IS 516 (BIS 1959). The cubes were tested for optimum dosage at 7

and 28 days of curing age. **Figure 3.16** shows the testing of concrete specimens for compression.

For each type of concrete mix, three cubes were tested. For the compressive strength of the concrete mix, the average value of three specimens was taken. The formula for calculating compressive strength is given in equation 2:

$$f_{ck} = P/A \quad (2)$$

Where,

A = 100×100×100 mm size of cube's surface area (mm^2)

P = Maximum load applied (N)

f_{ck} = Compressive strength (N/mm^2)

Figure 3.16 -Testing of specimen for compression in CTM

3.5 TESTS ON SMA AND CONCRETE

3.5.1 Bond Test

A mechanical bond test is a technique used in materials science and engineering to evaluate the strength and effectiveness of bonds between different materials. By subjecting the bonded materials to mechanical stress, the test determines the maximum force required to break or deform the bond. This information is crucial for assessing bond strength, optimizing bonding processes, selecting suitable materials, ensuring quality control, and conducting failure analysis. By understanding the performance of material bonds, engineers and scientists can make informed decisions to create safer, more reliable, and durable products in various industries.

3.5.1.1 Testing Methods

There are several testing methods commonly used in bond testing to evaluate the strength and quality of material bonds. Here are some of the main testing methods:

Tensile Testing: It is also known as pull testing, is a widely used method for bond testing. It involves applying a tensile force to the bonded materials in opposite directions, perpendicular to the bond interface. The force is gradually increased until the bond fails. Tensile testing provides information about the bond's resistance to pulling forces and measures the maximum force required to break the bond.

Many types of bond testing such as Shear testing evaluates bond strength by subjecting bonded materials to parallel shear stress, while peel testing measures bond strength by applying perpendicular force to cause one material to peel away from the other. Cleavage testing assesses bond strength within layered structures by separating the layers. Microscopy and imaging techniques visually inspect the bonded interface for defects, while non-destructive testing methods like ultrasonic testing and X-ray inspection evaluate bond quality without damaging the bond. The selection of a testing method depends on the bond type, materials used, and desired information, considering each method's advantages and limitations.

3.5.1.2 Factors Affecting Bond Strength

Several factors can significantly influence bond strength between materials, including surface preparation, adhesive selection, curing conditions, material compatibility, temperature and environmental factors, mechanical loads and stress concentrations, surface roughness and contact area, and processing techniques and parameters. These factors must be carefully considered and addressed to optimize bond strength, select appropriate materials, and ensure reliable and durable bonds. Each factor's importance may vary depending on the bonding application and specific requirements, but understanding and managing these factors are crucial for achieving strong and long-lasting bonds.

3.5.1.3 Applications and Importance of bond test

Bonding tests have significant applications and importance across various industries. They are used to assess the quality and strength of bonds in manufacturing and construction, automotive and aerospace components, electronics and microelectronics, medical devices, packaging, and consumer goods. Bonding tests ensure that products meet safety standards, performance requirements, and regulatory compliance. They play a vital role in optimizing bonding processes, selecting suitable materials, identifying weak points, and validating adherence to

industry standards. By conducting bonding tests, manufacturers can enhance product quality, minimize failure risks, and deliver reliable and durable products to consumers.

3.5.1.4 Limitations and Considerations

When conducting bond tests, it is important to consider limitations and factors that can impact the accuracy and interpretation of the results. These include the size and representativeness of the samples, the test speed and strain rate, the testing environment and conditions, the operator's skill and technique, adherence to test validation and standards, statistical analysis and interpretation, and the need for additional examination techniques for evaluating the bond interface. By carefully addressing these considerations, following protocols, and seeking expert guidance, more reliable and meaningful bond test outcomes can be obtained.

3.5.1.5 Preparation of Specimens

The preparation of specimens involves several steps to ensure the proper casting and curing of the concrete. The steps involved in the preparation are following;

Mold preparation: The molds to shape the concrete specimens are prepared. Cubical molds are used for compressive strength testing and bond testing which are cleaned and ensured to be free of any residue or previous concrete.

Material selection: The appropriate materials for the concrete mixture are selected. This includes aggregates (such as sand and gravel), cement, water, and polypropylene ether based superplasticizer.

Mixing: The concrete mixture is prepared by combining the selected materials in the correct proportions. A concrete mixer or mixing device is used to achieve a uniform and consistent blend. The mixing process is performed according to recognized standards or specific project requirements.

Mold coating: A thin layer of mold release agent or oil is applied to the inner surfaces of the molds. This prevents the concrete from sticking to the molds and facilitates the removal of the hardened specimens.

Casting: The freshly mixed concrete is filled into the molds in three layers. The concrete is evenly distributed and properly compacted within the molds to eliminate voids or segregation. After compaction of two layers by using a vibrating table, SMA fibre and steel fibre is embedded (40 mm) in the third layer of casting.

Demolding: After the specified curing period, which is 24 hours from the casting time the specimens are carefully removed from the molds. The molds are gently tapped or appropriate demolding techniques are used to release the specimens without causing any damage.

Curing: The concrete specimens are covered in a curing tank which is maintained at 27±2℃ for 28 days.

Storage and testing: The cured specimens are stored in a controlled environment until they reach the desired age for testing. The curing duration depends on the intended testing requirements.

Following recognized guidelines and standards, such as those provided by organizations like ASTM International, can ensure the accuracy and reliability of the prepared concrete specimens.

3.5.2 Test setup

In this study, cube specimens, resembling a 100 mm cube, with the fibers were used for pullout tests. The compressive strength of the cube was measured as 60 MPa. Each fiber had a length of 65 mm, and 40 mm of the length was embedded in the cube. The pullout test was conducted with the help of universal testing machine (UTM). It required a special arrangement to hold the cube and the fibre and then perform pull out motion. The arrangement consists of a 40 m long steel rod with the 4 mm diameter hole at one end with tightening screws to hold the fibre. The other part consist of a rectangular steel frame which can fit in a 100×100×100 mm cube with a hole on its upper face. Both of these components are then attached to the grips of the UTM in order to perform the tensile action.

(a) **(b)**

Figure 3.17 - (a) SMA marked for embedded length (b) Specimens for bond test

3.5.3 Pull out Test

The pull-out test is a method used to evaluate the bond strength between concrete and embedded reinforcement, such as steel bars or anchors or SMA bars. This test was performed in accordance with IS 2770 - Part 1 (BIS 1967). In this study, cube specimens, resembling a 100 mm cube, with the fibres were used for pullout tests. The compressive strength of the cube was measured as 60 MPa. Each fibre had a length of 65 mm, and 40 mm of the length was embedded in the cube. The pullout test was conducted with the help of a Universal Testing Machine (UTM). It required a special arrangement to hold the cube and the fibre and then perform pull out motion. The arrangement consists of a 40 cm long steel rod with the 4 mm diameter hole at one end with tightening screws to hold the fibre which is shown in **Figure 3.18 (b)**.

(a)

(b)

(c)

(d)

(e)

Figure 3.18 – Testing machine (a) Universal Testing Machine; (b) Sample set up; (c) Briquette type 1; (d) Briquette type 2; (e) Briquette type 3

The other part consist of a rectangular steel frame which can fit in a 100×100×100 mm cube with a hole on its upper face. Both of these components are then attached to the grips of the UTM in order to perform the tensile action. The force is gradually increased until the reinforcement either pulls out or breaks from the concrete. By measuring the maximum force required for pull-out, the test provides an indication of the bond strength between the reinforcement and the concrete. This information is crucial for assessing the structural integrity and load-carrying capacity of concrete elements, such as beams, columns, and slabs. The pull-out test is widely used in construction and engineering projects to ensure the quality and performance of concrete structures, as well as to verify compliance with design and safety standards.

3.5.3.1 Pull out Test Setup used by Various Researchers.

Baena et al. (2009)-The pull-out test setup, utilized a servo-hydraulic testing machine with a maximum capacity of 600 kN. Displacement control was employed to observe the behavior of the specimen after reaching the peak load. The load was applied to the reinforcement bar at a rate of 0.02 mm/s and measured using the electronic load cell integrated into the testing machine. The slip at both the loaded and unloaded ends of the specimen was measured using four linear variable differential transformers (LVDTs).

Choi et al. (2018) - In the pull-out test configuration, the bottom of the specimen was held by a half-circular holder, while the fiber was subjected to extraction using an actuator. The applied force during the test was measured by a load cell positioned on the machines cross head, while the slip between the fiber and the mortar was monitored using a linear voltage displacement transducer (LVDT) attached to the specimen. To maintain consistency, the test was conducted with displacement control at a speed of 1.0 mm/min, and data was recorded at a sampling rate of 5.0 Hz.

Hu Feng et al. (2019) -To investigate the behavior of fiber pullout, a modern electronic universal testing machine with a maximum load-bearing capability of 5 kN was utilized. This investigation aimed to understand the interaction between fibers and the matrix, composed of Magnesium Phosphate Cement (MPC). An extensometer was employed to measure the degree of slippage occurring between the fiber and the MPC matrix. During the pullout tests, the rate at which the loading was applied was standardized at 0.5 mm of slip per minute. To ensure statistical validity, each test group consisted of five individual specimens. All specimens within each group underwent the pullout testing procedure.

3.6 HIGH STRENGTH CONCRETE AT ELEVATED TEMPERATURES

Studying the behavior of high strength concrete and steel reinforcing bars under elevated temperatures is crucial not only for extreme fire events but also for structures that regularly experienced elevated temperatures. Examples include nuclear reactor pressure vessels, coal gasification and liquefaction vessels, petrochemical industry pressure vessels, and storage tanks for hot crude oil, hot water, and hot clinker.

When compared to normal strength concrete, high strength concrete exhibits different behavior under fire conditions. Its lower water-cement ratio results in lower porosity, making it more brittle and reducing its fire endurance at elevated temperatures. High strength concrete experiences a faster decline in compressive strength and elastic modulus, making it more susceptible to spalling. Therefore, when using high strength concrete in fire-resistant applications, its performance in fire conditions becomes a major concern.

Elevated temperatures lead to deformations and changes in material properties within structural members. By understanding these deformations and property changes, traditional structural mechanics methods can be applied to predict the fire resistance performance of structural members. Having material properties at elevated temperatures allows for a mathematical approach to predict the fire resistance of structural members made with high strength concrete. In the past, determining the fire resistance of structural members relied mainly on testing. However, in recent years, numerical and analytical methods for calculating the fire resistance of various structural members have gained wide acceptance. These calculation methods are more cost-effective and time-efficient compared to extensive testing procedures.

In order to examine how elevated temperatures affect the bond strength and weight of concrete, test samples were prepared and their initial weight was recorded. These samples were then placed inside a Rectangular Muffle Furnace, where they underwent controlled heating. The temperature inside the furnace was gradually increased at a rate of 10℃ per minute. The samples were exposed to three different temperature levels during the experiment: 200℃, 400℃, and 600℃. **Figure 3.19** and **3.20** illustrates the experimental setup and the progression of temperatures throughout the test. **Figure 3.21, 3.22, 3.23 and 3.24** shows the color changes and cracks develop after heating at the temperature of 200℃, 400℃ and 600℃.

Figure 3.19 Rectangular Muffle Furnace

(a) (b)

Figure 3.20 (a) Muffle furnace set at temperature of 600℃; (b) Samples kept in Furnace for heating.

(a) (b)

Figure 3.21 Concrete after heating of temperature of 600℃ (a) Top side of cube; (b) Bottom side of cube

(a) (b)

Figure 3.22 Concrete after heating of temperature of 400℃ - (a) Top side of cube; (b) Bottom side of cube

(a) (b)

Figure 3.23 Concrete after heating of temperature of 200℃- (a) Top side of cube; (b) Bottom side of cube

(a) (b) (c)

Figure 3.24 Cracks develop in concrete after heating of temperature at; (a) 200℃; (b) 400℃ (c) 600℃.

Concrete can develop cracks when exposed to critical temperature thresholds: 200, 400, and 600 degrees Celsius. These temperatures mark stages where concrete's strength deteriorates: at 200°C, cement paste weakens as water evaporates, leaving weaker cement particles; at 400°C, calcium hydroxide decomposes, producing water vapor and calcium carbonate, which weakens concrete and promotes cracking; at 600°C, cement paste melts, posing a severe threat to structural integrity. Although cracking can vary due to factors like composition and environment, these critical temperatures serve as valuable benchmarks. Factors beyond temperature, such as freezing, thawing, abrasion, and heavy loads, also contribute to cracking, yet the critical temperature thresholds remain significant influencers.

3.7 SAMPLES PREPARED AND TESTED FOR VARIOUS TESTS

The total number of samples prepared for experimental work would depend on various factors, such as the objectives of the study, the research methodology, and the statistical requirements for the analysis. Total samples prepared and tested for various tests as shown below in **Table 3.14.**

Table 3.14 Number of samples prepared and tested for tests.

Tests	Number of specimens prepared for tests.	Tested samples
Compressive test	68	68
Bond Test	26	19 (Fibres break in 7 samples during test)
Cement compressive test	6	6
Mass Loss Test	12	12
Tensile Test	2	2

The **Table 3.14** shows the number of specimens prepared for tests and the number of tested samples for four different types of tests.

- Compressive test: 42 specimens were prepared for the compressive test and 26 are for bond test but after pull out test compressive test also carried out on bond test samples, therefore total 68 specimens were tested.
- Bond test: 26 specimens were prepared for the bond test, but 7 of the specimens broke during the test may be because the fibers in the specimens were not strong enough, or the bond between the fibers and the concrete was not strong enough, or man handling. Therefore, only 19 specimens were tested.
- Cement compressive test: 6 specimens were prepared for the cement compressive test, and all 6 specimens were tested.
- Mass loss test: 12 specimens were prepared for the mass loss test, and all 12 specimens were tested at 200, 400 and 600 degree Celsius.
- Tensile Test of SMA: 2 samples are taken of 50 mm length and 0.53mm diameter for this test and all the samples are tested.

CHAPTER 4

RESULTS AND DISCUSSION

4.1 GENERAL

The main aim of the study is to analyze and compare the performance of two reinforcing materials, namely Shape Memory Alloy (SMA) and Steel fibers, when used in conjunction with high-strength concrete having a compressive strength of 60 MPa. The study involves conducting several tests to assess various aspects of the concrete mixes. i.e., Compressive strength of different mixes, Weight loss percentage at different temperatures, Bond strength between the concrete and fibres at different shapes, have been discussed.

4.2 COMPRESSIVE STRENGTH

4.2.1 Effect of different water to binder (w/c) ratios on the strength of Mapefill 05.

The values of the compressive strength of water cured samples of all the concrete sample mixes at the ages of 7, 28 and 56 days are shown in Table 4.1.

Table 4.1 Compressive strength values of water-cured concrete samples at different water to binder ratios for three different ages: 7 days, 28 days, and 56 days.

Testing age (days) ⟶ w/c ↓		**7**	**28**	**56**
0.11	CS (MPa)	41.72	47.9	50.51
0.13	CS (MPa)	45.37	49.06	52.76
0.14	CS (MPa)	47.2	55.175	60.36

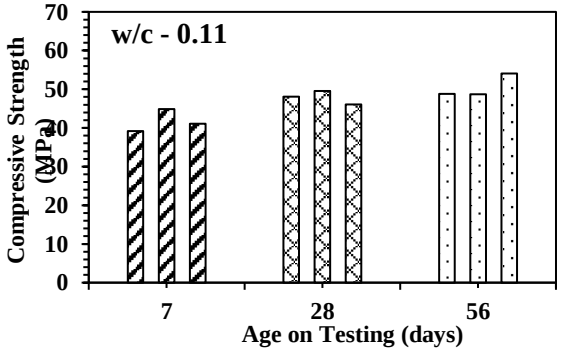

Figure 4.1 Compressive strength at 7, 28 and 56 days at w/c = 0.11 of Mapefill 05

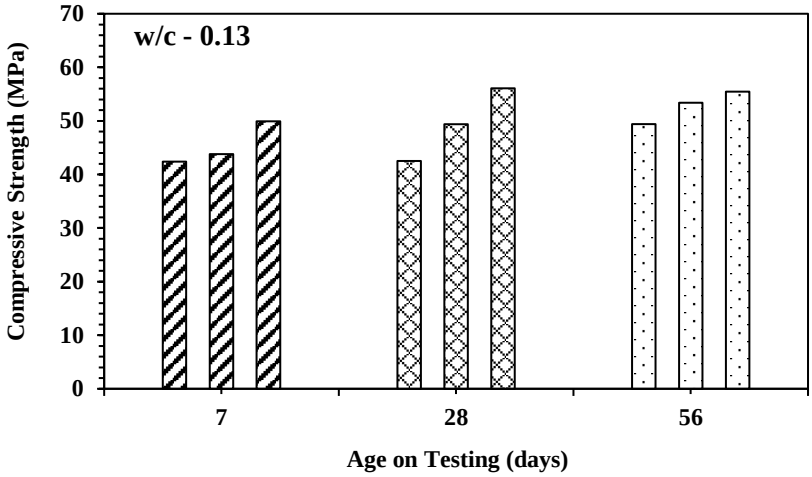

Figure 4.2 Compressive strength at 7, 28 and 56 days at w/b = 0.13 of Mapefill 05

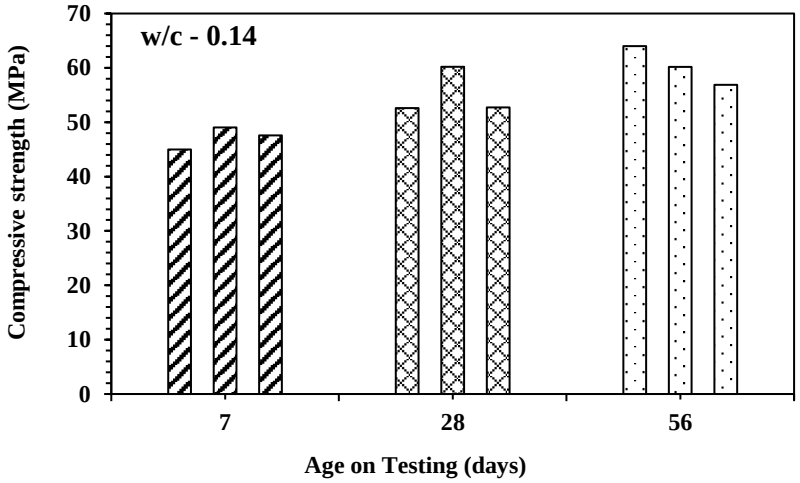

Figure 4.3 Compressive strength at 7, 28 and 56 days at w/b = 0.14 of Mapefill 05

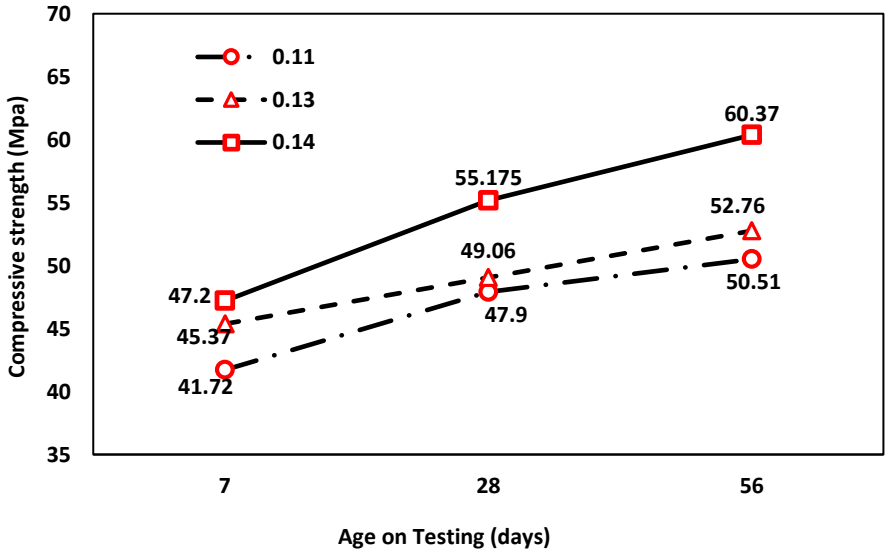

Figure 4.4 Trend line of compressive strength at 7, 28 and 56 days for different w/b ratio.

4.1.2 Effect of water curing on the compressive strength of concrete mixes (Mapefill 05)

The values of the compressive strength of water cured samples of all the concrete mixes at the ages of 7, 28 and 56 days are shown in Table 4.2. The positive sign shows the gain in strength while the negative sign shows the loss in strength.

Table 4.2 Effect of water curing on compressive strength with different w/b mixes of Mapefill 05.

Testing age (days)⟶ W/c ↓		**7**	**28**	**56**
0.11	CS (MPa)	41.72	47.9	50.51
	% change	-	-	-
0.13	CS (MPa)	45.37	49.06	52.76
	% change	+8.74	+2.42	+4.45
0.14	CS (MPa)	47.2	55.175	60.36
	% change	+13.13	+15.18	+19.5

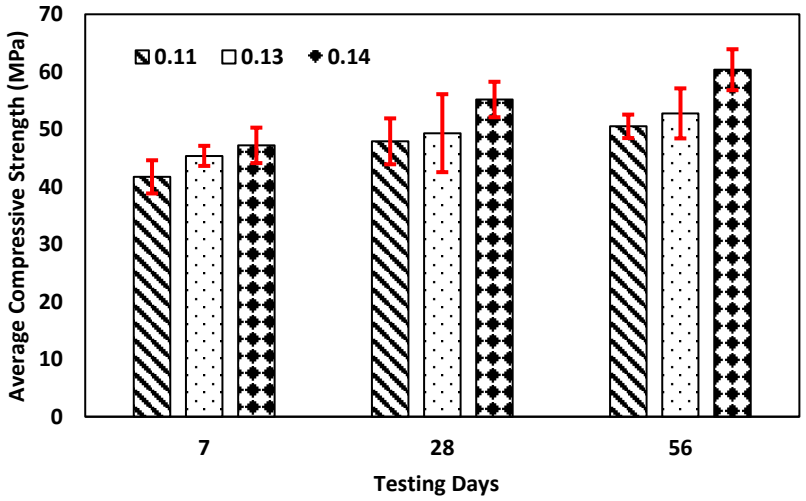

Figure 4.5 Comparison of compressive strength at 7, 28 and 56 days for different w/b ratio of Mapefill 05

From the above tables, we can conclude that the compressive strength data of Mapefill 05 reveals interesting trends across different water-binder ratios and testing ages. For the mix with a water binder ratio of 0.11, there is a notable percentage increase in compressive strength from 7 days to 56 days, ranging from approximately 21.2% to 21.0%, respectively. Similarly, for the

mix with a ratio of 0.13, the percentage increase in strength ranges from approximately 8.8% to 13.2% during the same period. In contrast, the mix with a water binder ratio of 0.14 displays a relatively significant percentage increase in strength, varying from approximately 17.5% to 27.8% from 7 days to 56 days. These findings suggest that different water-cement ratios influence the rate of strength development, with higher ratios leading to more pronounced strength gains over time.

Mapefill 05, containing cement as its key binder material, undergoes a hydration process when water is added during mixing. This chemical reaction leads to the formation of calcium silicate hydrate (C-S-H) gel and calcium hydroxide ($Ca(OH)_2$). These gel formations contribute to binding the aggregate particles, resulting in a cohesive and solid material. The compressive strength of Mapefill 05 is found to be highest in the mix with a water-cement (w/c) ratio of 0.14, which strikes a better balance between workability and strength development. On the other hand, mixes with w/c ratios of 0.13 and 0.11 may exhibit lower strength due to challenges in mixing and compacting a mix with limited water content, despite potentially having lower porosity. Selecting an appropriate w/c ratio is crucial to achieve optimal workability and strength in Mapefill 05.

4.1.3 The Effect of water curing on compressive strength of final mix of HSC of 60 MPa.

Table 4.3 Compressive strength trial on HSC of 60 MPa.

Testing age (days) →		**7**	**28**	**56**
W/c ↓				
0.29	CS (MPa)	40.5	60.6	62.45

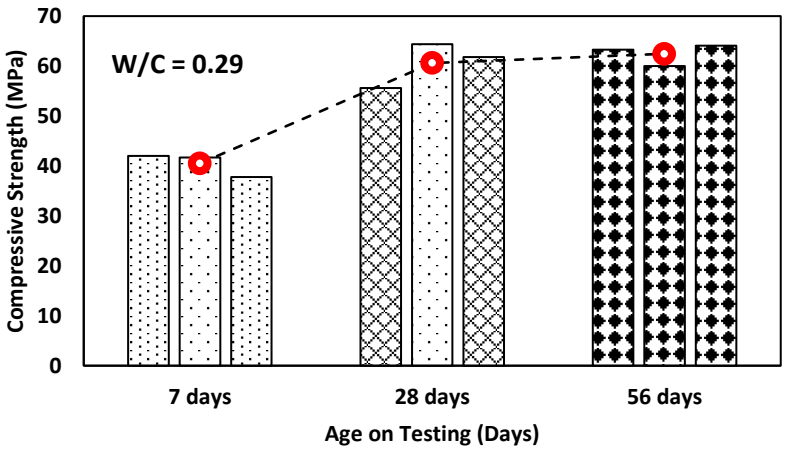

Figure 4.6 compressive strength at 7, 28 and 56 days for target strength of M60.

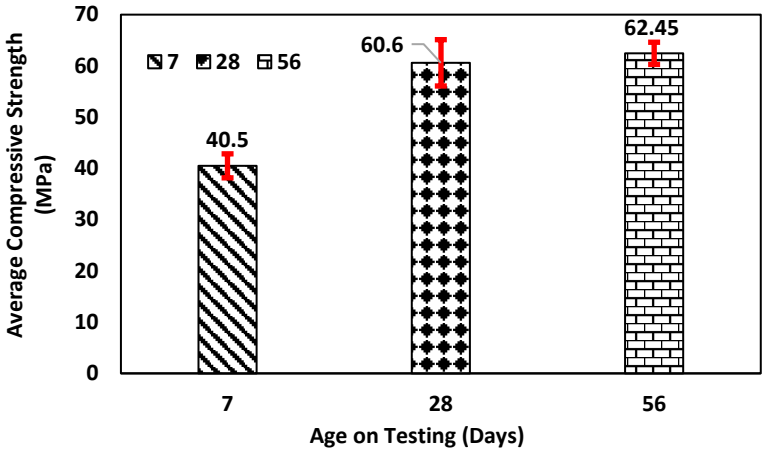

Figure 4.7 Average compressive strength at 7, 28 and 56 days for target strength of M60.

From **Table 4.3** data we can say that the compressive strength trial on the High-Strength Concrete (HSC) mix with a target strength of 60 MPa reveals a notable development in strength over time. The concrete mix demonstrated a steady increase in compressive strength as the curing period progressed. Starting with a strength of 40.5 MPa at 7 days, it reached the desired target strength of 60 MPa at 28 days, indicating successful achievement of the specified requirement. The influence of the water-to-cement ratio (w/c) was evident, as the lower w/c ratio of 0.29 resulted in slightly lower early-age strength at 7 days, but ultimately contributed to higher strength development at 28 days and beyond. This finding underscores the importance of proper curing practices, as the concrete exhibited significant improvements in strength over time.

Overall, the results demonstrate the suitability of the HSC mix with a w/c ratio of 0.29 for various structural applications that demand high compressive strength. The concrete's performance beyond the target age of 28 days was particularly noteworthy, with a compressive strength of 62.45 MPa at 56 days, indicating the potential for further strength enhancement over extended curing periods. These findings provide valuable insights for optimizing the mix design and ensuring the HSC's reliable performance in applications where meeting and exceeding the specified target strength are essential factors for success.

4.2 WEIGHT LOSS AT DIFFERENT TEMPERATURES.

The investigation of mass loss at various temperatures (200°C, 400°C, and 600°C) holds significant importance as it sheds light on the response of high-strength concrete specimens, which have been reinforced with SMA fibers, when exposed to elevated temperatures. This analysis involves placing the concrete samples inside a specialized Muffle furnace, where they are subjected to heightened temperatures for a specific time frame of 3 hours, with a

meticulously controlled heating rate of 10°C per minute. This crucial assessment aids in understanding the concrete's capacity to endure relatively extreme conditions, which can be encountered in certain construction scenarios or during fire incidents.

Table 4.4 Average weight loss percentage at different temperatures.

Temperatures (°C) → Testing age ↓	**200**	**400**	**600**
3 hrs.	3.261	4.676	5.959

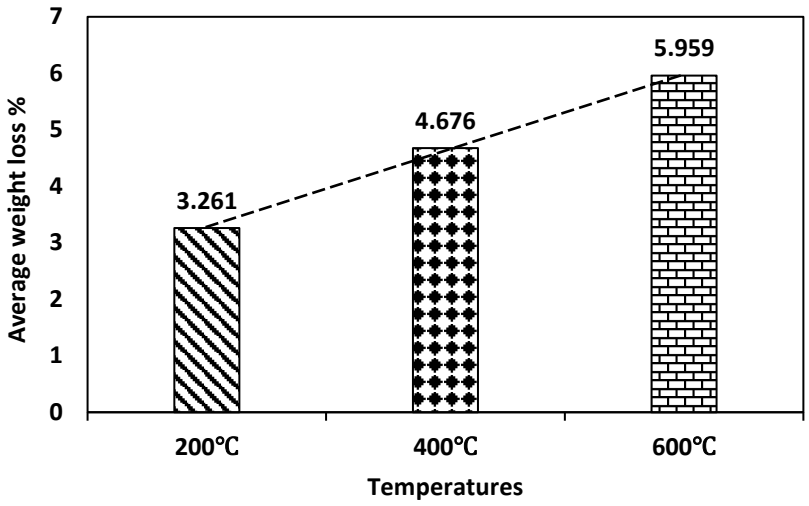

Figure 4.8 Average weight loss percentage at 200°C, 400°C and 600°C.

The data from **Table 4.4** clearly demonstrates that as the temperature rises, the weight loss of the high-strength concrete specimen increases gradually. From 200°C to 400°C and further to 600°C, the mass loss percentages show a discernible upward trend, with the highest mass loss occurring at 600°C, indicating that extreme temperatures significantly impact the material's weight. However, despite the higher temperatures, the SMA wire's presence, embedded to a length of 40 mm, proves effective in reinforcing the concrete and maintaining its structural integrity to some extent. Observing **Figure 4.8**, the evident linear trend line indicates that the mass loss of concrete samples at distinct temperatures (200°C, 400°C, and 600°C) maintains a consistent pattern. This suggests that as the temperature increases, the reduction in mass follows a predictable path. This finding holds substantial implications for comprehending the material's response to elevated temperatures and its process of deterioration when exposed to heat.

4.3 EFFECT OF DIFFERENT END SHAPE ON PULL OUT BETWEEN FIBRE AND HSC OF 60 MPa.

Table 4.5 Results of SMA Pull out Test

Type	P_{max} (N)	σ_{max}(MPa)	δ (mm)	τ_{max} (MPa)
H/T1/1	700	3173.16	1.6	6.46
H/T1/2	400	1813.23	1.67	3.69
H/T1/3	1100	4986.4	2.69	10.16
Average	**733.33**	**3324.26**	**1.98**	**6.77**
H/T2/1	200	906.18	1.63	1.84
H/T2/2	3700	16772.44	0.83	34.18
H/T2/3	200	906.18	4.06	1.84
Average	**1366.67**	**6194.93**	**2.17**	**12.62**
H/T3/1	1200	5439.71	4.58	11.08
H/T3/2	100	453.3	2.13	0.92
H/T3/3	3500	15865.82	3.79	32.34
H/T3/4	500	2266.54	2.4	4.62
Average	**1325**	**6006.34**	**3.225**	**12.24**
H/TC/1	700	3173.16	2.17	6.46
Average	**700**	**3173.16**	**2.17**	**6.46**
S/TC/1	300	1359.92	0.33	2.77
S/TC/2	500	2266.54	0.26	4.62
Average	**400**	**1813.23**	**0.295**	**3.695**
SS/TC/1	100	453.3	0.27	0.92
SS/TC/2	100	453.3	0.32	0.92
SS/TC/3	100	453.3	0.54	0.92
Average	**100**	**453.3**	**0.376**	**0.92**
SH/TC/1	3400	15412.5	0.32	31.41
SH/TC/2	100	453.3	0.34	0.92
SH/TC/3	100	453.3	0.55	0.92
Average	**1200**	**5439.7**	**0.403**	**11.083**

The provided **Table 4.5** presents a comprehensive set of data related to various mechanical properties and behaviors of different types of specimens subjected to different conditions. The table includes information on maximum pull-out load (P_{max}), corresponding pull-out stress (σ_{max}), displacement (δ), and maximum bond strength (τ_{max}) is calculated by using eq. (3). The types of specimens include different SMA configurations (H/T1, H/T2, H/T3, H/TC, S/TC), as well as other materials and configurations (SS/TC, SH/TC).

H/T1, H/T2, H/T3, H/TC, S/TC: These are different types of hooked and straight Shape Memory Alloy (SMA) specimens tested at various temperatures (200°C, 400°C, 600°C and room temperature), where H represent Hooked SMA and S represent Straight SMA.
SS/TC, SH/TC: These are different types of specimens, including Steel straight at room temperature (SS/TC) and Steel hooked at room temperature (SH/TC).

Maximum Bond Strength is calculated by using this formula,

$$\tau_{max} = P_{max}/\pi d_f L_{em} \quad \text{..... (3)}$$

Where,
P_{max} is maximum Pull out load in (N).
d_f is diameter of fibre and
L_{em} is length of embedment of fibre in concrete.

Conclusions from Table 4.5 :

- **Effect of Temperature on SMA**: When comparing the Hooked SMA specimens (H/T1, H/T2, H/T3) tested at different temperatures, it's evident that higher temperatures generally result in higher maximum pull-out loads, pull-out stresses, and bond strengths. This suggests that the material's performance improves at elevated temperatures, likely due to altered mechanical properties and structural changes.

- **Influence of Temperature on Steel Specimens**: The data for different steel specimens (SS/TC, SH/TC) at room temperature indicates that the hooked steel specimens (SH/TC) exhibit significantly higher maximum pull-out loads, pull-out stresses, and bond strengths compared to the other steel configurations. This highlights the beneficial effects of shape and temperature on bond strength.

- **Comparing Different Specimen Types**: When comparing the average values for the different specimen types, the Hooked SMA at 600°C (H/T3) shows the highest

maximum pull-out load, pull-out stress, and bond strength. This might imply that this specific configuration is the strongest among those tested.

- **Temperature-Dependent Behavior**: The increase in bond strength with higher temperature suggests that the materials' bonding characteristics improve under elevated temperature conditions. However, it's important to further investigate the underlying mechanisms causing these variations.

- **Impact of Shape and Material**: The hooked SMA specimens consistently demonstrate higher bond strengths and mechanical properties compared to steel specimens. This showcases the potential advantages of using SMA and specifically the hooked configuration for enhancing bond strength.

4.3.1 Pull out behavior of Hooked end SMA at 200°C

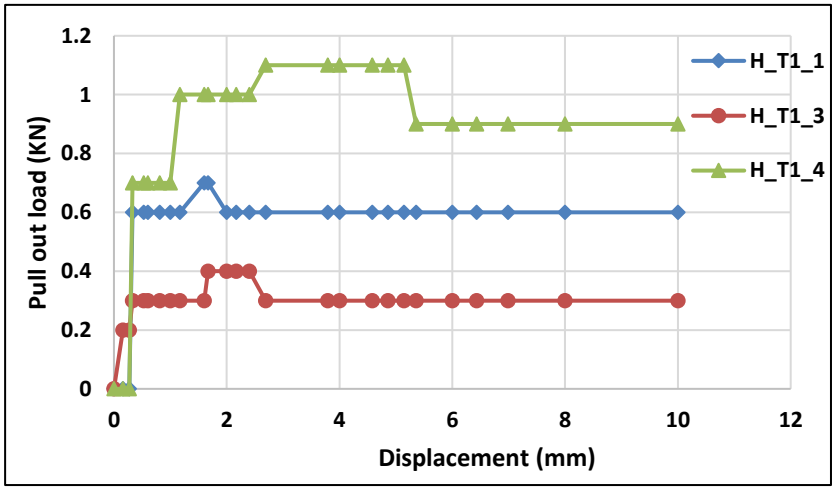

Figure 4.9 Pull out load vs displacement graph at 200°C

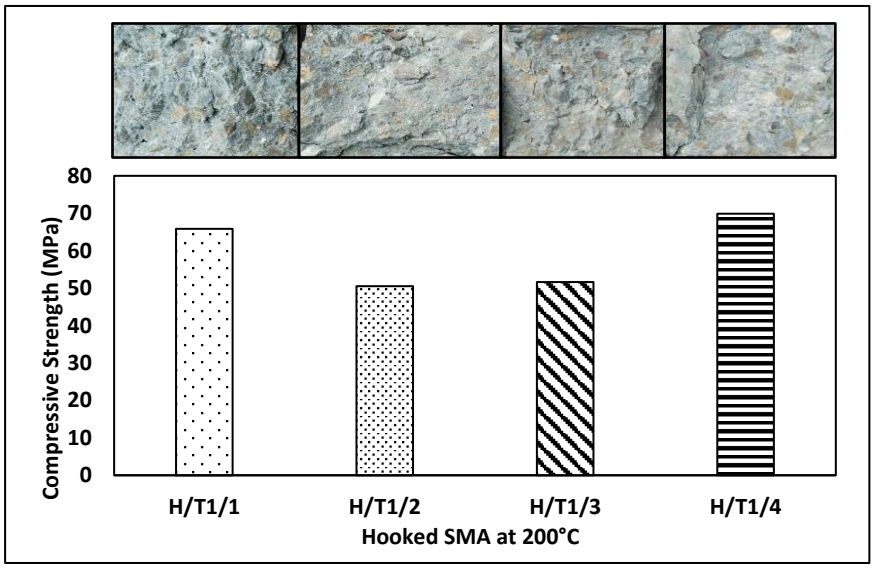

Figure 4.10 Compressive strength and packing of samples at 200°C

Based on the information presented in **Figure 4.9**, it's evident that the highest pullout loads observed at temperature of 200°C for the samples are 0.7 kN, 0.4 kN, and 1.1 kN, corresponding to the samples labeled as H/T1/1, H/T1/3, and H/T1/4, respectively. These pullout loads represent the maximum force required to remove the samples from their positions. Additionally, the corresponding displacements at which these maximum pullout loads occur are 1.6 mm, 1.67 mm, and 2.69 mm for the respective samples. This information underscores the strength and stability of the samples at different pullout loads, helping to better understand their performance under the specified conditions.

4.3.2 Pullout behavior of Hooked end SMA at 400°C

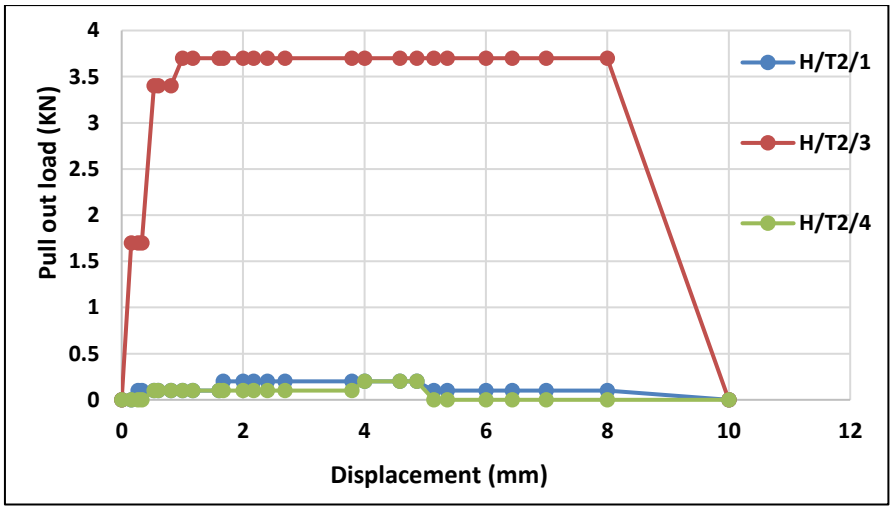

Figure 4.11 Pull out load vs displacement graph at 400°C

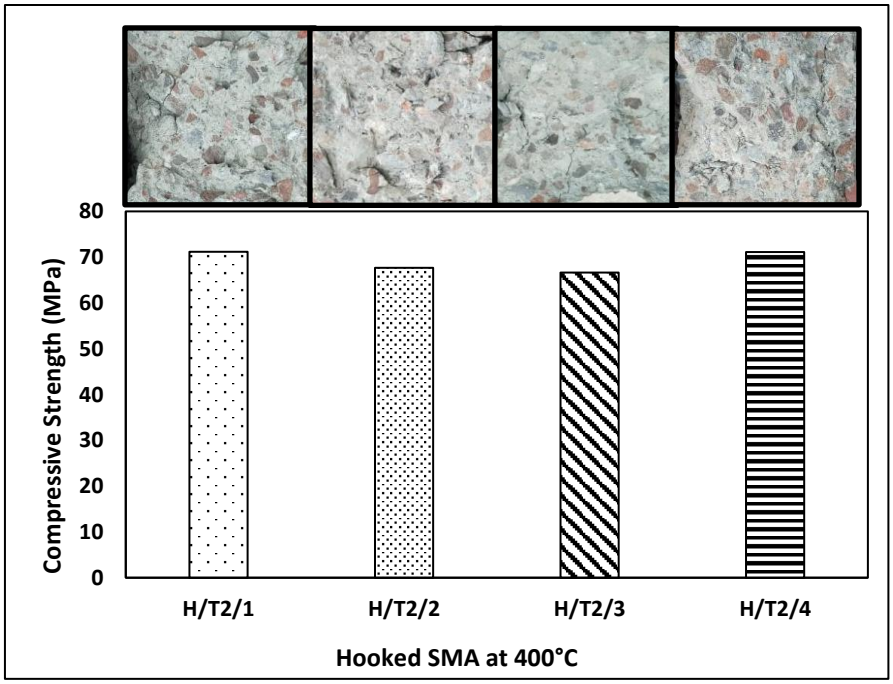

Figure 4.12 Compressive strength of samples at 400°C

Based on the information presented in **Figure 4.11**, it's evident that the highest pullout loads observed at a temperature of 400°C for the samples are 0.2 kN, 3.7 kN, and 0.2 kN, corresponding to the samples labeled as H/T2/1, H/T2/3, and H/T2/4, respectively. These pullout loads represent the maximum force required to remove the samples from their positions. Additionally, the corresponding displacements at which these maximum pullout loads occur are 1.67 mm, 1 mm, and 4 mm for the respective samples.

4.3.3 Pullout behavior of Hooked end SMA at 600º C

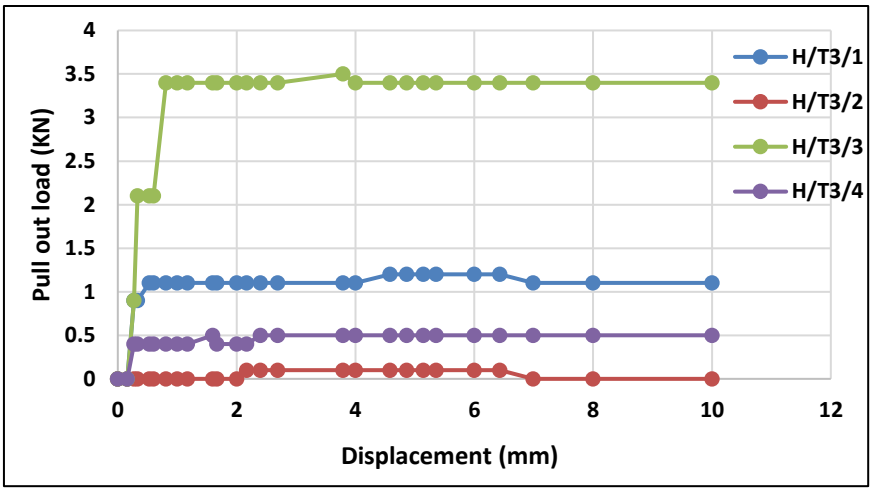

Figure 4.13 Pull out load vs displacement graph at 600°C

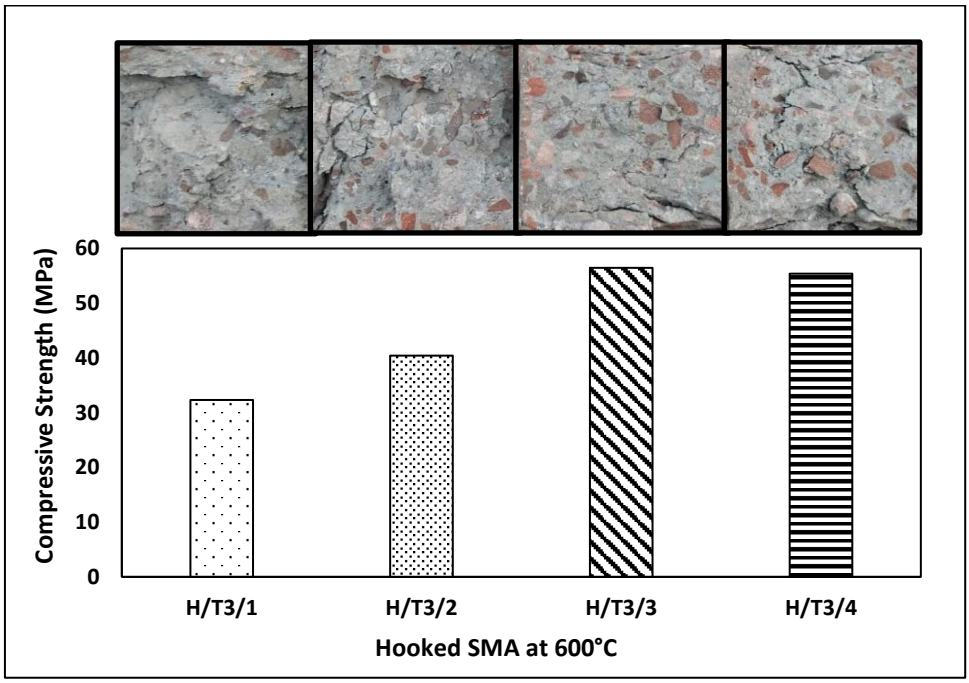

Figure 4.14 Compressive strength and packing of samples at 600°C

Based on the information presented in **Figure 4.13**, it's evident that the highest pullout loads observed at temperature a of 600°C for the samples are 1.2 kN, 0.2 kN, 3.4 KN and 0.5 kN,

corresponding to the samples labeled as H/T3/1, H/T3/2, H/T3/3 and H/T3/4, respectively. These pullout loads represent the maximum force required to remove the samples from their positions. Additionally, the corresponding displacements at which these maximum pullout loads occur are 4.58 mm, 2.17 mm, 0.81mm and 1.6 mm for the respective samples.

4.3.4 Pull out behavior of Hooked end SMA at room temperature.

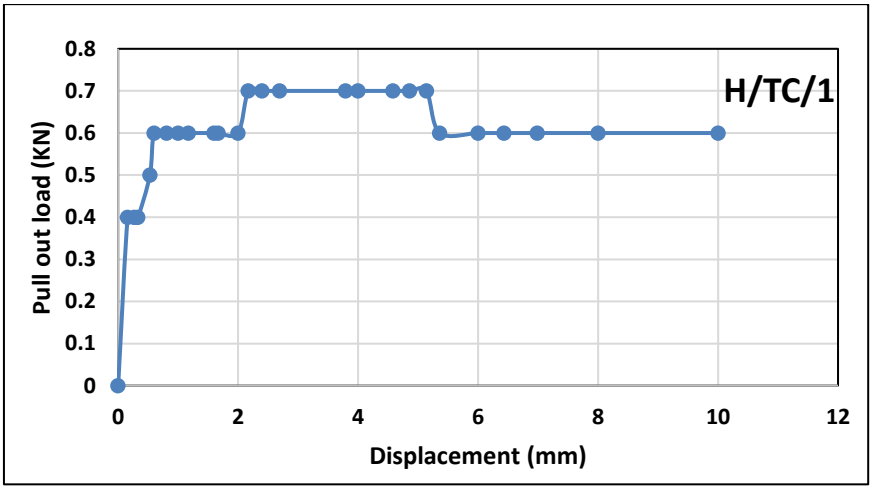

Figure 4.15 Pull out load vs displacement graph at room temperature

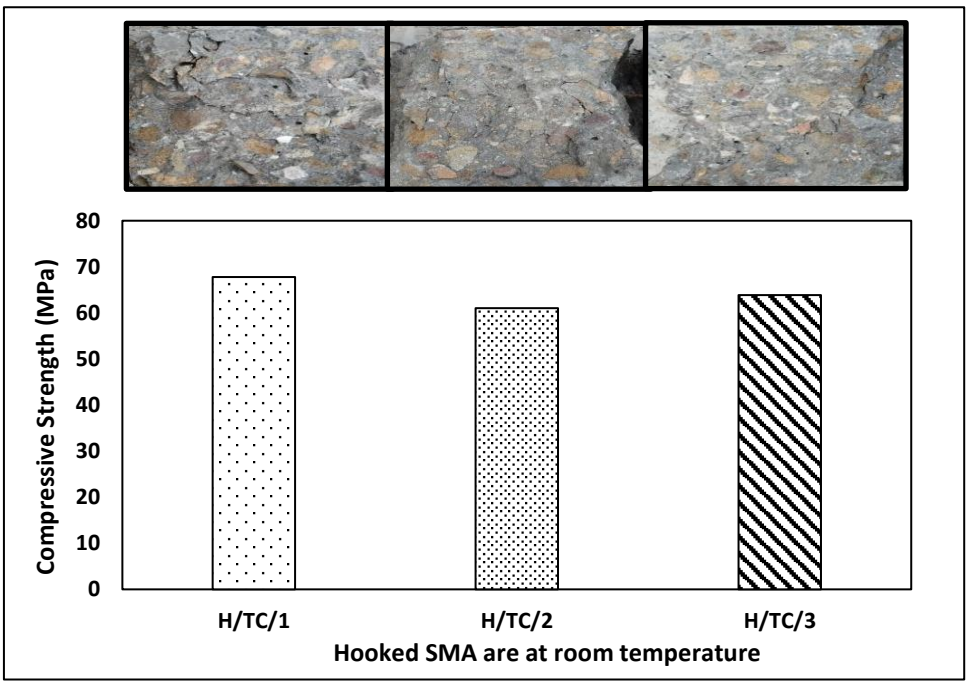

Figure 4.16 Compressive strength and packing of samples at room temperature

Based on the information presented in **Figure 4.15**, it's evident that the highest pullout load observed at room temperature for the sample is 0.7 kN corresponding to the sample labeled as H/TC/1. The pullout load represents the maximum force required to remove the sample from its position. Additionally, the corresponding displacement at which the maximum pullout load

occurred is 2.17 mm and **Figure 4.16** shows the compressive strength and its packing of the concrete, it helps to correlate the strength and bond of the structure.

4.3.5 Pull out behavior of Straight end SMA at room temperature

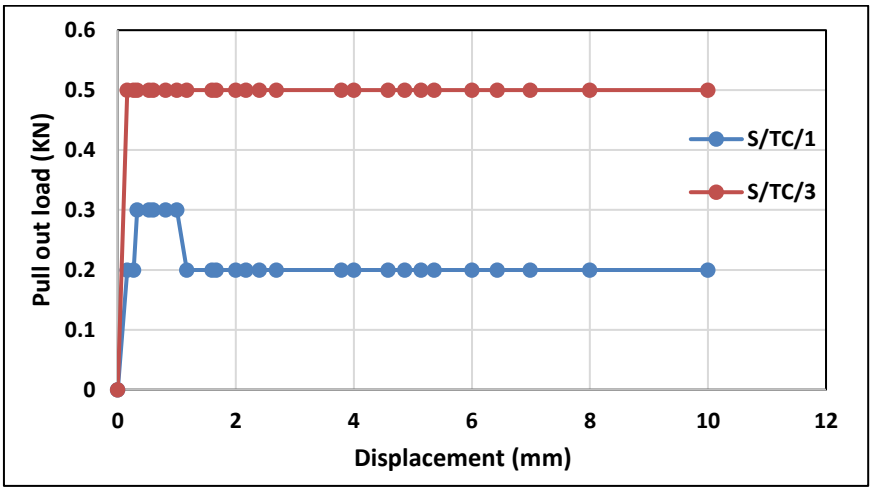

Figure 4.17 Pull out load vs displacement graph at room temperature

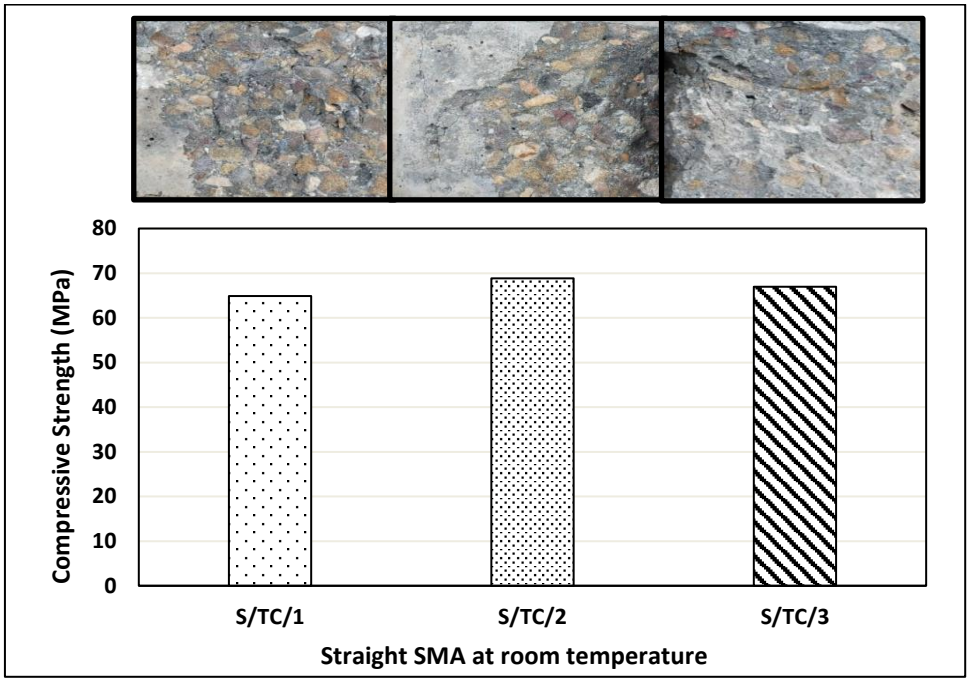

Figure 4.18 Compressive strength of straight SMA samples at room temperature

Based on the information presented in **Figure 4.17**, it's evident that the highest pullout loads observed at room temperature for the sample are 0.3 and 0.5 kN corresponding to the samples labeled as S/TC/1 and S/TC/3 respectively. These pullout loads represent the maximum force required to remove the samples from their positions. Additionally, the corresponding displacements at which these maximum pullout loads occurred are 0.33 and 0.16 mm for the respective sample and **Figure 4.18** shows the compressive strength and its packing of the concrete, it helps to correlate the strength and bond of the structure.

4.3.6 Pull out behavior of Straight and Hooked end Steel at room temperature

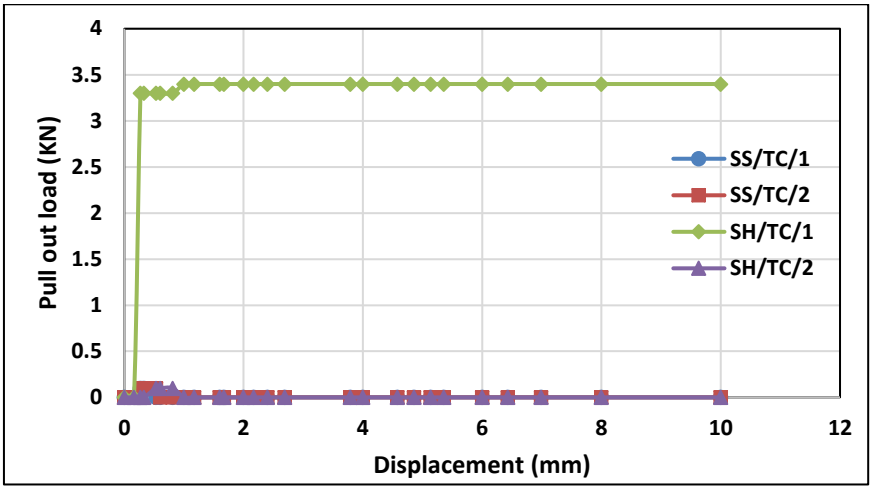

Figure 4.19 Pull out load vs displacement graph at room temperature

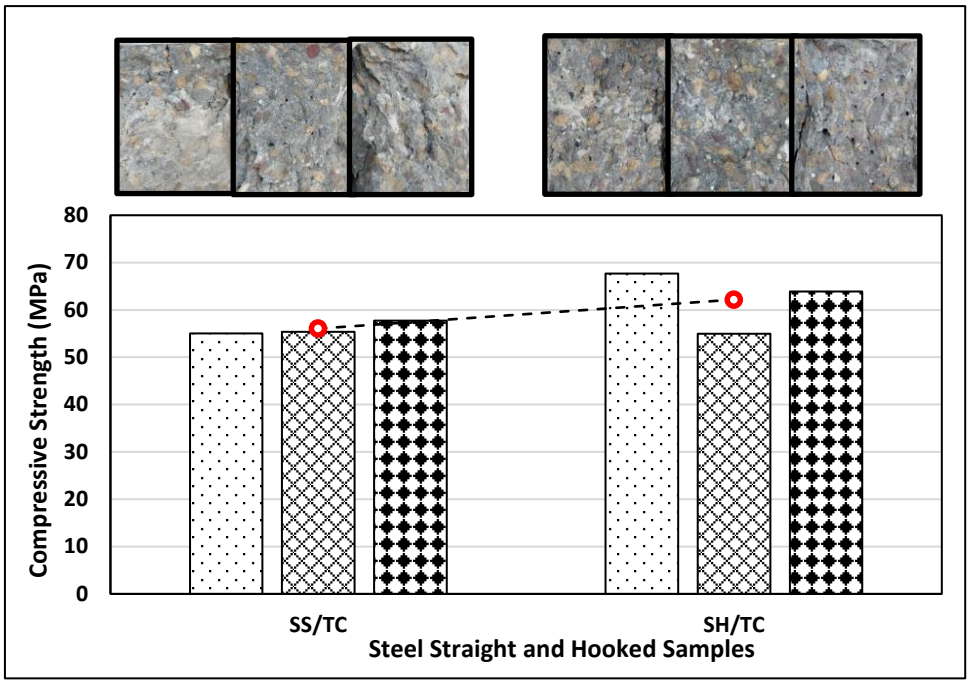

Figure 4.20 Compressive strength and packing of samples at room temperature; (a) SS/TC/1; (b) SS/TC/2; (c) SS/TC/3; (d) SH/TC/1; (e) SH/TC/2; (f) SH/TC/3

Based on the information presented in **Figure 4.19**, it's evident that the highest pullout loads observed at room temperature is 0.1KN for both samples labeled as SS/TC/1 and SS/TC/2, which is straight end shaped steel samples and 3.4 kN and 0.1 kN are the highest pull out loads labeled as SH/TC/1 and SH/TC/2 respectively. These pullout loads represent the maximum force required to remove the samples from their positions. Additionally, the corresponding displacements at which these maximum pullout loads occur are the same and value is 0.27 mm for straight shape and 1, 0.53 are for hooked end steel shape for the respective sample and Figure 4.20 shows the compressive strength and its packing of the concrete, it helps to correlate the strength and bond of the structure.

4.4 COMPRESSIVE STRENGTH OF SAMPLES AT DIFFERENT TEMPERATURES AFTER PULL OUT TESTING.

The results of the pull-out tests revealed a range of pull-out strength values for the concrete specimens. Similarly, the compressive strength tests provided a distribution of compressive strength values. A statistical analysis was conducted to explore any potential correlation between the two sets of results. While some degree of correlation might be observed in specific cases, it is evident that pull-out strength cannot be solely relied upon as an indicator of compressive strength due to the complex interplay of factors affecting both properties.

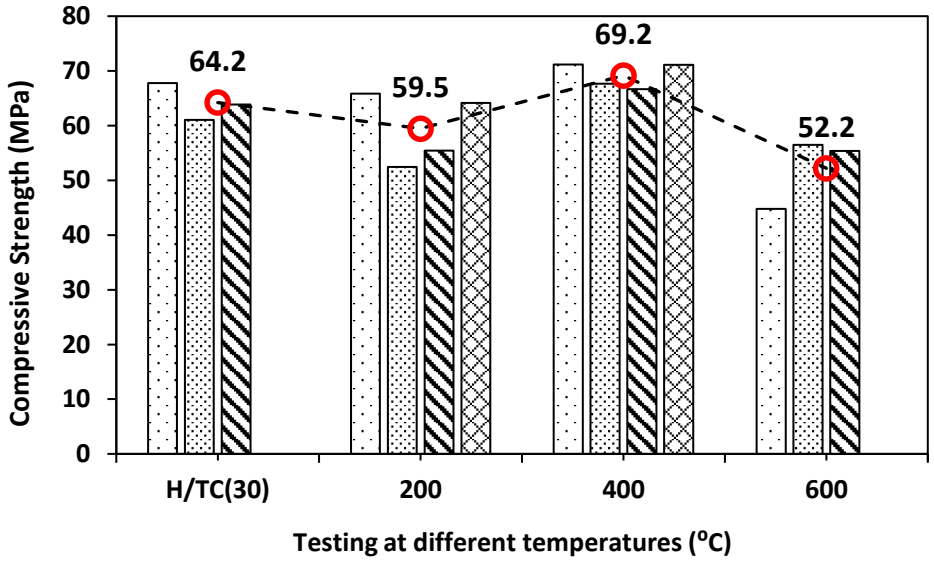

Figure 4.21 Compressive strength vs Testing at different temperatures of Hooked SMA samples

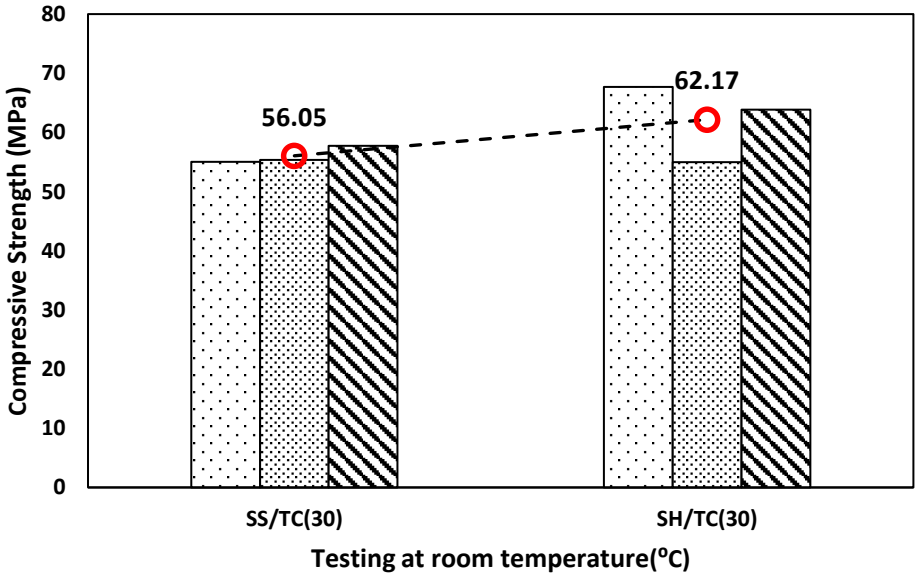

Figure 4.22 Compressive strength vs Testing at room temperatures of steel samples

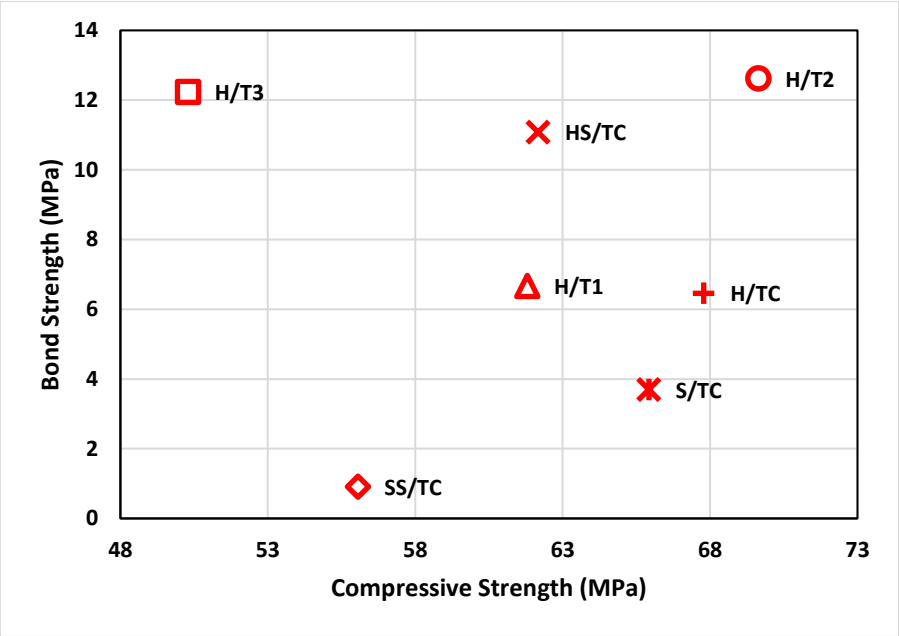

Figure 4.23 Bond Strength versus Compressive Strength of SMA and steel samples at different temperatures.

As depicted in **Figure 4.23**, the compressive strength analysis underscores notable disparities among different SMA configurations. The most substantial average compressive strength of 69.64 is evident in the case of H/T2 (hooked SMA at 400°C), showcasing the advantageous impact of elevated temperature treatment. In contrast, the weakest average compressive strength, registering at 50.29, is observed in H/T3 (hooked SMA at 600°C), suggesting potential vulnerabilities at extreme temperatures. H/T1 (hooked SMA at 200°C) and H/TC (hooked SMA at room temperature) exhibit comparable average compressive strengths of 61.8 and 67.78, respectively, shedding light on the significance of both the hooking process and ambient temperature conditions. Notably, S/TC (straight SMA at room temperature) demonstrates an average compressive strength of 65.92, aligning within the range of other configurations. So we can conclude that the compressive strength appears to vary with the temperature at which the SMA is hooked. H/T2 (400°C) exhibits the highest compressive strength, possibly due to optimal micro structural properties resulting from its elevated temperature treatment. The decrease in compressive strength observed for H/T3 (600°C) could be due to possible changes in the material's micro structure, leading to reduced strength. Comparatively, H/TC and S/TC show relatively higher compressive strengths, suggesting that the hooking process or straight configuration might enhance the material's compressive performance.

Based on the information presented in **Figure 4.23**, an analysis of bond strength reveals distinct trends among different SMA configurations. Notably, the most substantial average bond

strength of 12.62 is evident in H/T2 (hooked SMA at 400°C), indicating the beneficial impact of higher temperature processing. In contrast, the lowest average bond strength, measuring 3.695, is observed in the case of S/TC (straight SMA at room temperature), suggesting limitations in bonding mechanisms without the hooking process. Meanwhile, H/T1 (hooked SMA at 200°C), H/TC (hooked SMA at room temperature), and H/T3 (hooked SMA at 600°C) exhibit bond strengths of 6.77, 6.46, and 12.24, respectively. So we can conclude that the bond strength seems to vary significantly between the different configurations. H/T2 (400°C) again exhibits the highest bond strength, indicating effective adhesion or interlocking due to the hooking process at this temperature. S/TC, the straight SMA at room temperature, has the lowest bond strength, which could be attributed to the absence of additional bonding mechanisms like hooking. H/T3 (600°C) also shows a relatively high bond strength, suggesting that the material's properties at this temperature might promote strong bonding.

4.5 TENSILE TESTING OF SMA

Table 4.6 Data of Pull out load and its corresponding displacement.

	Tensile 1				Tensile 2		
1	0	0	0.16	1	0	0	0.17
2	20	0.1	0.33	2	20	0.1	0.34
3	40	0.1	0.49	3	40	0.1	0.51
4	60	0.1	0.65	4	60	0.1	0.68
5	80	0.1	0.82	5	80	0.1	0.85
6	100	0.1	0.99	6	100	0.1	1.02
7	120	0.1	1.16	7	120	0.1	1.19
8	140	0.1	1.31	8	140	0.1	1.36
9	160	0.1	1.48	9	160	0.1	1.52
10	180	0.1	1.66	10	180	0.1	1.69
11	200	0.1	1.82	11	200	0.1	1.86
12	220	0.1	1.99	12	220	0.1	2.03
13	240	0.1	2.16	13	240	0.1	2.19
14	260	0.1	2.33	14	260	0.1	2.36
15	280	0.1	2.49	15	280	0.2	2.52
16	300	0.2	2.67	16	300	0.2	2.7
17	320	0.2	2.84	17	320	0.2	2.86
18	340	0.2	3.01	18	340	0.2	3.03
19	360	0.2	3.17	19	360	0.2	3.19
20	380	0.2	3.34	20	380	0.2	3.37
21	400	0.2	3.51	21	400	0.2	3.54
22	420	0.2	3.68	22	420	0	3.71
23	440	0.2	3.85				
24	460	0.2	4.02				
25	480	0.2	4.19				
26	500	0.2	4.36				
27	520	0	4.53				

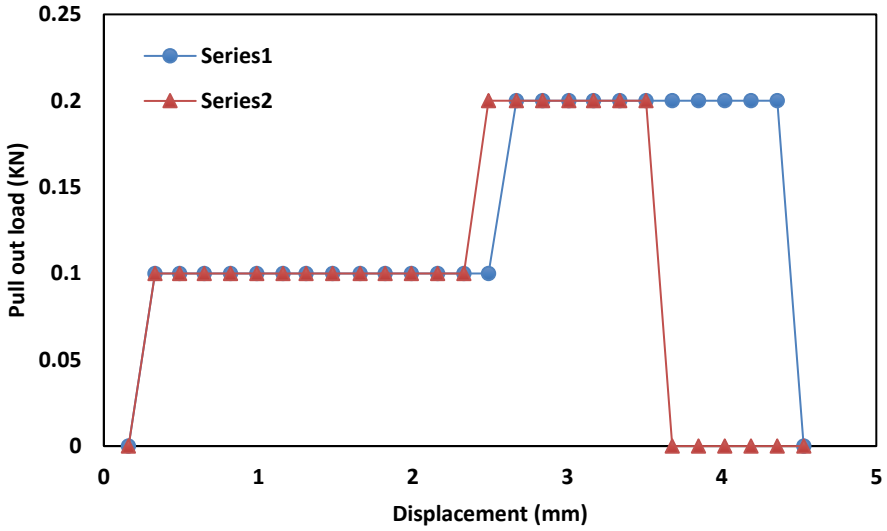

Figure 4.24 Displacement versus pull out load of SMA fiber (T1,T2)

As depicted in Figure 4.24, the results obtained from the tensile testing of Shape Memory Alloy (SMA) samples show consistent patterns in how the material behaves under stress. As the samples are pulled apart, the force needed increases along with the amount they stretch, demonstrating that the material becomes tougher to stretch as it experiences more deformation. This matches what we typically see in tensile tests, where you need more force to stretch something further. First, there's a straight-line relationship between the force applied and how much the samples stretch, indicating the SMA's ability to bounce back to its original shape after the force is removed. But as we look at more data points, this straight-line pattern changes, suggesting that the material starts changing its shape in a more permanent way after a certain point—this is the yield point, where it begins to undergo permanent changes when stretched. After that, the relationship between force and stretch becomes more complex, showing that even when we stop applying force, the material remains changed. The highest point in the data represents the maximum force the SMA can handle before it breaks. Past this point, the material starts getting weaker, leading to an eventual fracture. Another important thing we can learn is how much the material can deform before breaking, which tells us if it's flexible (ductile) or more prone to just snapping (brittle). All of these findings together give us a clear picture of how the SMA responds to being pulled and how we might use it in engineering.

CHAPTER 5

CONCLUSIONS

5.1 COMPRESSIVE STRENGTH AND WEIGHT LOSS ANALYSIS AT ELEVATED TEMPERATURES OF HSC OF 60 MPa.

The investigation of the compressive strength of HSC with a target strength of 60 MPa confirmed the successful attainment of the desired strength level. The concrete mix design and materials used in the study demonstrated their effectiveness in producing high-strength concrete, which is crucial for various structural applications where superior load-bearing capacity is required. The investigation of weight loss at elevated temperatures (200°C, 400°C, and 600°C) demonstrated the remarkable resilience of SMA fibre-reinforced HSC to extreme thermal conditions. The SMA fibre unique shape memory effect played a crucial role in mitigating deformation and limiting additional damage, making the reinforced HSC resilient to elevated temperatures up to 600°C.

5.2 BOND STRENGTH EVALUATION

Assessing the bond strength between fibers and high-strength concrete (HSC) with a 60 MPa compressive strength yielded significant insights into fiber performance as reinforcement. Results highlighted variations in bond strength based on fiber end shapes. Similarly, the examination of bond strength within various Shape Memory Alloy (SMA) configurations emphasized the influential roles of temperature treatment, hooking processes, and micro structural changes in shaping bonding mechanisms. These insights are essential for informed decision-making in the design and incorporation of SMA reinforced concrete elements, effectively enhancing structural robustness and long-term durability.

5.3 RECOMMENDATIONS FOR FUTURE RESEARCH

As this study focused on specific aspects of SMA fibers in high-strength concrete, there are opportunities for further research to deepen our understanding of these materials' behavior. Future studies could explore the influence of performance of the SMA fibers for different end shapes, fiber orientation, and design strength of concrete on the overall performance of SMA reinforced concrete. Further, cyclic response can be obtained, which helps us to know about the energy absorption and hysteresis behavior of fibers. Additionally, extending research to encompass cyclic heating of concrete would present an avenue to enhance our understanding of the impact of prolonged thermal exposure on the chemical composition of concrete.

REFERENCES

Song, G., Ma, N., & Li, H. N. (2006). Applications of shape memory alloys in civil structures. *Engineering structures*, *28*(9), 1266-1274.

Ozbulut, O. E., Hurlebaus, S., & DesRoches, R. (2011). Seismic response control using shape memory alloys: a review. *Journal of Intelligent Material Systems and Structures*, *22*(14), 1531-1549.

Zareie, S., & Zabihollah, A. (2020). Hysteresis Behavior of Pre-Strained Shape Memory Alloy Wires Subject to Cyclic Loadings: An Experimental Investigation. *Emerging Trends in Mechatronics*, 151.

Gu, X., Yu, Y., Li, Y., Li, J., Askari, M., & Samali, B. (2019). Experimental study of semi-active magnetorheological elastomer base isolation system using optimal neuro fuzzy logic control. *Mechanical Systems and Signal Processing*, *119*, 380-398.

Chen, P. C., Tsai, K. C., & Lin, P. Y. (2014). Real-time hybrid testing of a smart base isolation system. *Earthquake engineering & structural dynamics*, *43*(1), 139-158.

Fu, W., Zhang, C., Li, M., & Duan, C. (2019). Experimental investigation on semi-active control of base isolation system using magnetorheological dampers for concrete frame structure. *Applied Sciences*, *9*(18), 3866.

Rabiee, R., & Chae, Y. (2019). Adaptive base isolation system to achieve structural resiliency under both short-and long-period earthquake ground motions. *Journal of Intelligent Material Systems and Structures*, *30*(1), 16-31.

Dezfuli, F. H., & Alam, M. S. (2014). Performance-based assessment and design of FRP-based high damping rubber bearing incorporated with shape memory alloy wires. *Engineering Structures*, *61*, 166-183.

Tabrizikahou, A., Kuczma, M., Łasecka-Plura, M., Farsangi, E. N., Noori, M., Gardoni, P., & Li, S. (2022). Application and modelling of Shape-Memory Alloys for structural vibration control: State-of-the-art review. *Construction and Building Materials*, *342*, 127975.

Jani, J. M., Leary, M., Subic, A., & Gibson, M. A. (2014). A review of shape memory alloy research, applications and opportunities. *Materials & Design (1980-2015)*, *56*, 1078-1113.

Saiidi, M. S., & Wang, H. (2006). Exploratory study of seismic response of concrete columns with shape memory alloys reinforcement. *ACI Materials Journal*, *103*(3), 436.

Saiidi, M. S., O'Brien, M., & Sadrossadat-Zadeh, M. (2009). Cyclic Response of Concrete Bridge Columns Using Superelastic Nitinol and Bendable Concrete. *ACI Structural Journal*, *106*(1).

Andrawes, B., Shin, M., & Wierschem, N. (2010). Active confinement of reinforced concrete bridge columns using shape memory alloys. *Journal of Bridge Engineering*, *15*(1), 81-89.

Yang, C. S. W., DesRoches, R., & Leon, R. T. (2010). Design and analysis of braced frames with shape memory alloy and energy-absorbing hybrid devices. *Engineering Structures*, *32*(2), 498-507.

Speicher, M., Hodgson, D. E., DesRoches, R., & Leon, R. T. (2009). Shape memory alloy tension/compression device for seismic retrofit of buildings. *Journal of materials engineering and performance*, *18*, 746-753.

Ma, H., & Cho, C. (2008). Feasibility study on a superelastic SMA damper with re-centring capability. *Materials Science and Engineering: A*, *473*(1-2), 290-296.

van de Lindt, J. W., & Potts, A. (2008). Shake table testing of a superelastic shape memory alloy response modification device in a wood shearwall. *Journal of structural engineering*, *134*(8), 1343-1352.

Li, H., Mao, C. X., & Ou, J. P. (2008). Experimental and theoretical study on two types of shape memory alloy devices. *Earthquake engineering & structural dynamics*, *37*(3), 407-426.

Han, Y. L., Xing, D. J., Xiao, E. T., & Li, A. Q. (2005). NiTi-wire shape memory alloy dampers to simultaneously damp tension, compression, and torsion. *Journal of Vibration and Control*, *11*(8), 1067-1084.

DesRoches, R., Taftali, B., & Ellingwood, B. R. (2010). Seismic performance assessment of steel frames with shape memory alloy connections. Part I—analysis and seismic demands. *Journal of Earthquake Engineering*, *14*(4), 471-486.

Sepúlveda, J., Boroschek, R., Herrera, R., Moroni, O., & Sarrazin, M. (2008). Steel beam–column connection using copper-based shape memory alloy dampers. *Journal of Constructional Steel Research*, *64*(4), 429-435.

Youssef, M. A., Alam, M. S., & Nehdi, M. (2008). Experimental investigation on the seismic behavior of beam-column joints reinforced with superelastic shape memory alloys. *Journal of Earthquake Engineering*, *12*(7), 1205-1222.

Alam, M. S., Youssef, M. A., & Nehdi, M. (2008). Analytical prediction of the seismic behaviour of superelastic shape memory alloy reinforced concrete elements. *Engineering Structures*, *30*(12), 3399-3411.

Ma, H., Wilkinson, T., & Cho, C. (2007). Feasibility study on a self-centering beam-to-column connection by using the superelastic behavior of SMAs. *Smart Materials and Structures*, *16*(5), 1555.

Ocel, J., DesRoches, R., Leon, R. T., Hess, W. G., Krumme, R., Hayes, J. R., & Sweeney, S. (2004). Steel beam-column connections using shape memory alloys. *Journal of Structural engineering*, *130*(5), 732-740.

Huang, B., Lao, Y., Chen, J., & Song, Y. (2018). Dynamic response analysis of a frame structure with superelastic nitinol SMA helical spring braces for vibration reduction. *Journal of Aerospace Engineering*, *31*(6), 04018096.

Cortés-Puentes, W. L., & Palermo, D. (2018). Seismic retrofit of concrete shear walls with SMA tension braces. *Journal of Structural Engineering*, *144*(2), 04017200.

Gao, N., Jeon, J. S., Hodgson, D. E., & DesRoches, R. (2016). An innovative seismic bracing system based on a superelastic shape memory alloy ring. *Smart materials and structures*, *25*(5), 055030.

Zhu, S., & Zhang, Y. (2008). Seismic analysis of concentrically braced frame systems with self-centering friction damping braces. *Journal of Structural Engineering*, *134*(1), 121-131.

Zhou, Z., Xie, Q., Meng, S. P., Wang, W. Y., & He, X. T. (2016). Hysteretic performance analysis of self-centering buckling restrained braces using a rheological model. *Journal of Engineering Mechanics*, *142*(6), 04016032.

Huang, B., Song, Y., Wu, Y., Lao, Y., & Song, G. (2018, April). Experimental Analysis of the Pseudoelasticity of Nitinol Shape Memory Alloy Helical Springs. In *16th Biennial International Conference on Engineering, Science, Construction, and Operations in Challenging Environments* (pp. 844-856). Reston, VA: American Society of Civil Engineers.

Huang, H., Mosalam, K. M., & Chang, W. S. (2020). Adaptive tuned mass damper with shape memory alloy for seismic application. *Engineering Structures*, *223*, 111171.

Mishra, S. K., Gur, S., & Chakraborty, S. (2013). An improved tuned mass damper (SMA-TMD) assisted by a shape memory alloy spring. *Smart Materials and Structures*, *22*(9), 095016.

Ozbulut, O. E., & Silwal, B. (2014, April). Performance of isolated buildings with superelastic-friction base isolators under high seismic hazards. In *Structures Congress 2014* (pp. 1967-1977).

Sutou, Y., Omori, T., Kainuma, R., & Ishida, K. (2008). Ductile Cu–Al–Mn based shape memory alloys: general properties and applications. *Materials Science and Technology*, *24*(8), 896-901.

Bouazaoui, L., & Li, A. (2008). Analysis of steel/concrete interfacial shear stress by means of pull out test. *International Journal of Adhesion and Adhesives*, *28*(3), 101-108.

Qian, H., Wu, P., Ren, Z., Chen, G., & Shi, Y. (2023). Pseudo-static tests of reinforced concrete pier columns confined with pre-tensioned superelastic shape memory alloy wires. *Engineering Structures*, *280*, 115680.

Hoult, R., & de Almeida, J. P. (2022). From experimental strain and crack distributions to plastic hinge lengths of RC walls with SMA rebars. *Engineering Structures*, *268*, 114731.

Wang, Y., Aslani, F., & Liu, Y. (2020). The effect of tensile and bond characteristics of NiTi shape memory alloy, steel and polypropylene fibres on FRSCC beams under three-point flexural test. *Construction and Building Materials*, *233*, 117333.

Feng, H., Sheikh, M. N., Hadi, M. N., Feng, L., Gao, D., & Zhao, J. (2019). Pullout behaviour of different types of steel fibres embedded in magnesium phosphate cementitious matrix. *International Journal of Concrete Structures and Materials*, *13*(1), 1-17.

Choi, E., Mohammadzadeh, B., Hwang, J. H., & Kim, W. J. (2018). Pullout behavior of superelastic SMA fibers with various end-shapes embedded in cement mortar. *Construction and Building Materials*, *167*, 605-616.

Sherif, M. M., Khakimova, E. M., Tanks, J., & Ozbulut, O. E. (2018). Cyclic flexural behavior of hybrid SMA/steel fiber reinforced concrete analyzed by optical and acoustic techniques. *Composite Structures*, *201*, 248-260.

Abdallah, S., Fan, M., Zhou, X. et al. (2016).Anchorage Effects of Various Steel Fibre Architectures for Concrete Reinforcement. *International Journal of Concrete Structures and Materials*, 10, 325–335.

Choi, E., Kim, D., Chung, Y. S., & Nam, T. H. (2014). Bond–slip characteristics of SMA reinforcing fibers obtained by pull-out tests. *Materials research bulletin*, *58*, 28-31.

Choi, E., Kim, Y. W., Chung, Y. S., & Yang, K. T. (2010). Bond strength of concrete confined by SMA wire jackets. *Physics Procedia*, *10*, 210-215.

Choi, E., Nhan, B. T., & Choi, J. (2023). Active SMA Fibers' Effect on the Pullout Behavior of a Steel Bar Embedded in Concrete. *Materials*, *16*(5), 1947.

Rodinò, S., Curcio, E. M., Renzo, D. A., Sgambitterra, E., Magarò, P., Furgiuele, F. & Maletta, C. (2022). Shape Memory Alloy—Polymer Composites: Static and Fatigue Pullout Strength under Thermo-Mechanical Loading. *Materials*, *15*(9), 3216.

Choi, E., Kim, H. S., & Nam, T. H. (2020). Effect of crimped SMA fiber geometry on recovery stress and pullout resistance. *Composite Structures*, *247*, 112466.

Abdallah, S., Fan, M., & Rees, D. W. (2018). Bonding mechanisms and strength of steel fiber–reinforced cementitious composites: Overview. *Journal of Materials in Civil Engineering*, *30*(3), 04018001.

Kim, D. J., Kim, H. A., Chung, Y. S., & Choi, E. (2016). Pullout resistance of deformed shape memory alloy fibers embedded in cement mortar. *Journal of Intelligent Material Systems and Structures*, *27*(2), 249-260.

Baena, M., Torres, L., Turon, A., & Barris, C. (2009). Experimental study of bond behaviour between concrete and FRP bars using a pull-out test. *Composites Part B: Engineering*, *40*(8), 784-797.

Markovich, I., Van Mier, J. G. M., & Walraven, J. C. (2001). Single fiber pullout from hybrid fiber reinforced concrete. *HERON, vol. 46 (3), 2001*.

Haddad, R. H., & Shannis, L. G. (2004). Post-fire behavior of bond between high strength pozzolanic concrete and reinforcing steel. *Construction and Building Materials*, *18*(6), 425-435.

Lublóy, É., & György, B. L. (2014). Temperature effects on bond between concrete and reinforcing steel. *Zbornik radova Građevinskog fakulteta, Subotica*, (26), 27-35.

Khalaf, J., & Huang, Z. (2016). Analysis of the bond behavior between prestressed strands and concrete in fire. *Construction and Building Materials*, *128*, 12-23.

BIS 12269:1987. "53 grade ordinary Portland cement [CED 2: Cement and Concrete]". *Bureau of Indian Standards (BIS)*, New Delhi, India.

IS 4031(part11):1988. "Methods of physical tests for hydraulic cement, Part 11: Determination of density". *Bureau of Indian Standards (BIS)*, New Delhi, India.

IS 4031(Part 5):1988. "Methods of physical tests for hydraulic cement, Part 5: Determination of initial and final setting times". *Bureau of Indian Standards (BIS)*, New Delhi, India.

IS 4031(Part 6):1988. "Methods of physical tests for hydraulic cement, Part 5: Determination of Compressive strength of hydraulic cement other than masonry cement". *Bureau of Indian Standards (BIS)*, New Delhi, India.

IS 383:1970. "Specification for Coarse and Fine Aggregates From Natural Sources For Concrete [CED 2: Cement and Concrete]". *Bureau of Indian Standards (BIS)*, New Delhi, India.

IS 9103:1999. "Specification for Concrete Admixtures - [CED 2: Cement and Concrete]". *Bureau of Indian Standards (BIS)*, New Delhi, India.

EN 1992-1-1 (2004) (English): Eurocode 2: Design of concrete structures - Part 1-1: General rules and rules for buildings.

IS 10262:2019. "Specification for Method of Preparation of Mix calculations of Concrete". *Bureau of Indian Standards (BIS)*, New Delhi, India.

IS 516:1959. "Method of Tests for Strength of Concrete [CED 2: Cement and Concrete]". *Bureau of Indian Standards (BIS)*, New Delhi, India.

IS 2770 (part 1):1967. "Methods of testing bond in reinforced concrete, Part 1: Pull-out test [CED 2: Cement and Concrete]." *Bureau of Indian Standards (BIS)*, New Delhi, India.

IS 1199 (part 2):2018. "Fresh concrete – Methods of sampling, testing and analysis, Part 2: Determination of consistency of Fresh Concrete." *Bureau of Indian Standards (BIS)*, New Delhi, India.

Document Information

Analyzed document	Deepak Raj_Thesis2023.pdf (D172449038)
Submitted	7/29/2023 6:38:00 PM
Submitted by	Trishna Choudhury
Submitter email	trishna.choudhury@thapar.edu
Similarity	4%
Analysis address	trishna.choudhury.thapar@analysis.urkund.com

Sources included in the report

SA	**Thesis.docx** Document Thesis.docx (D40240522)	2
SA	**_AnjaliTiwariStudy the Mechanical properties of UHPFRC.docx** Document _AnjaliTiwariStudy the Mechanical properties of UHPFRC.docx (D117938931)	1
SA	**FYP 2.pdf** Document FYP 2.pdf (D141971246)	2
SA	**Thesis Ambika D.docx** Document Thesis Ambika D.docx (D24027972)	1
SA	**Amit Kumar Thakur.docx** Document Amit Kumar Thakur.docx (D162387585)	1
SA	**FULL THESIS - SYAZA NUR IYLIA.pdf** Document FULL THESIS - SYAZA NUR IYLIA.pdf (D159139072)	6
SA	**FYP 2_TENGKU JASSHANIF BIN TENGKU ABDUL JALIL_2020744943_OURIGINAL REQ.pdf** Document FYP 2_TENGKU JASSHANIF BIN TENGKU ABDUL JALIL_2020744943_OURIGINAL REQ.pdf (D156707031)	5
SA	**Final copy.docx** Document Final copy.docx (D158853032)	1
SA	**Numerical study of the column reinforced with shape memory alloy.docx** Document Numerical study of the column reinforced with shape memory alloy.docx (D102622826)	1
SA	**FYP1_TENGKU JASSHANIF BIN TENGKU ABDUL JALIL_2020744943.pdf** Document FYP1_TENGKU JASSHANIF BIN TENGKU ABDUL JALIL_2020744943.pdf (D141557314)	1
SA	**C1 to C6 (31.01.docx** Document C1 to C6 (31.01.docx (D47565538)	2